Dynamics of Crowded and Active Biological Systems

by

Michael W. Stefferson

B.S., University of Arizona, 2012

M.S., University of Colorado, 2015

A thesis submitted to the

Faculty of the Graduate School of the

University of Colorado in partial fulfillment

of the requirements for the degree of

Doctor of Philosophy

Department of Physics

2018

This thesis entitled:
Dynamics of Crowded and Active Biological Systems
written by Michael W. Stefferson
has been approved for the Department of Physics

_____

Professor Meredith Betterton

_____

Professor Attendant Rank Matthew Glaser

_____

Assistant Professor Loren Hough

_____

Associate Professor Franck Vernerey

_____

Professor Attendant Rank Joseph MacLennan

Date _____

The final copy of this thesis has been examined by the signatories, and we find that both the content and the form meet acceptable presentation standards of scholarly work in the above mentioned discipline.

Stefferson, Michael W. (Ph.D., Physics)

Dynamics of Crowded and Active Biological Systems

Thesis directed by Professor Meredith Betterton

My abstract

Dedication

To someone.

Acknowledgements

My acknowledgements.

Contents

Chapter

Tables

Table

Figures

Figure

Chapter 1

Introduction

Interactions—either between particles or with the environment— ~~can~~ play a crucial role in the dynamics of biological systems. For example, there are biological polymeric filters which facilitate the transport of molecules, nanoparticles, viruses and other organisms through interactions between the polymers and particles [1]. In biological crowded media, obstacles can inhibit motion and introduce anomalous subdiffusion [2]. This has implications on the motion of lipids or macromolecules in membranes [3–10] and the cell interior [11]. Active matter systems—*e.g.*, a bacterial swarm [12–14]—can exhibit an array of exotic phenomena: dynamical phases, self assembly, and collective motion [15] because of the interplay between particle-particle interactions and ~~a~~ nonequilibrium activity. Understanding how microscopic interactions influence particle dynamics, transport, and macroscopic phases could assist in designing and tuning these systems.

The commonality ~~which unifies~~ these crowded and active systems is Brownian motion. A particle is considered Brownian if it undergoes ~~some seemingly~~ random motion in an environment— typically called a heat bath. The heat bath exerts two forces on the Brownian particle: random fluctuating force and frictional drag [16]. Note, the term heat bath, solvent, and solution will be interchangeably to describe the surrounding fluid environment ~~the particle is submerged in~~. Brownian motion was first reported by Robert Brown in 1927 when he observed he random motion of pollen in water. Einstein's interpretation that the phenomena could be described by water molecules bumping into the pollen provided further evidence of the existence of atoms and molecules [17]. ~~The underlying picture is a larger particle called a colloid, tracer, or Brownian particle—gets~~

bombarded by smaller solvent particles. If we knew all the trajectories of a solvent particles, we could calculate the motion of the Brownian particle. However, the degrees of the freedom are untrackable. Instead, we approximate the effect of the constant bumping of the solvent particles as providing a random fluctuating and damping force. The equation which describes this motion is the Langevin equation [16]. In most cases, we are interested in the overdamped limit which gives us Brownian dynamics (BD).

The study of Brownian dynamics is ubiquitous in physics and is used to describe a plethora of phenomena: diffusion of holes and electrons in semiconductors [18], Doppler cooling of neutral atoms [19], and motion of macromolecules in biological systems [20]. The primary focus of this thesis is analyzing different Brownian systems found in biological and other soft matter systems. We will examine the role of binding and bound motion in crowded environments, the transport of proteins across the nuclear pore complex (NPC), and active matter systems. Along the way, we will discuss the essential tools of computations and theoretical biophysicists: Brownian dynamics simulations, lattice Monte Carlo models, kinetic Monte Carlo, and numerical analysis of partial differential equations. I will describe how I implemented and advanced these tools to study various biological systems.

In this chapter, I will layout the essential principles of Brownian dynamics. After setting the foundation, we are ready to ask some questions this thesis hopes to answer. Namely, what are the effects of obstacles, particle particle interaction, and activity on tracer dynamics? We are interested in how we can study macroscopic behavior like transport and dynamical phases starting from a microscopic picture.

In this thesis, I will begin by first discussing various Brownian systems and providing the essential theory. I will then discuss a lattice Monte Carlo model which studied the effects of binding and bound motion on diffusion in a crowded environment [21]—results which have implications on various biological systems. Next, we will discuss transport across biofilters like the nuclear pore complex (NPC). I will present a minimalistic reaction diffusion equation which can predict the selectivity—what proteins can and cannot easily pass through—of the NPC in terms of measurable

parameters. I then move to active matter systems: nonequilibrium systems which can convert some source of stored energy into kinetic motion [15]. I will discuss how to derive macroscopic equations of motion starting from microscopic interactions using dynamic density functional theory (DDFT) [22–25], and how a pseudo-spectral theory was implemented to numerically evaluate them. Finally, I will apply this theory to a system of self-propelled hard needles and conclude ~~with discuss future work and perspectives~~.

1.1   Brownian dynamics

The equations of motion from a particle in a one dimensional heat bath is given by the Langevin equation [16]

$$m\dot{v} = \zeta v - \frac{dU}{dx} + \xi(t),$$ (1.1)

where ζ is the drag coefficient, U is the potential energy, and ξ is a random fluctuating force with properties

$$\langle \xi(t) \rangle = 0 \qquad \langle \xi(t)\xi(t') \rangle = 2\zeta k_B T \delta(t - t').$$ (1.2)

Here, we assumed that the drag is isotropic (same in all directions) and homogeneous (constant in space), and ignore hydrodynamic interactions between particles. We can recognize the Langevin equation as Newton's second law with forces from gradients in potential energy (from external fields and interactions) and the drag and a random force provided by the heat bath. ~~We will notice that~~ the drag and random force are connected through the drag coefficient (Eqn. 1.1 and 1.2. ~~The fact that these are entangled together~~ is a consequence of the fluctuation-Dissipation theorem [16] which is derived for ~~the~~ Brownian motion in Appx. A.

To understand the overdamped limit, ~~let's~~ assume the particle experiences a constant force f when an external field and temporarily ignore the random force. ~~By dropping ζ, we are looking at what happens to~~ the velocity on average. We can solve the linear ordinary differential equation for the velocity to v to get

$$v(t) = f/\zeta + e^{-\zeta t/m}\left[v(0) - f/\zeta\right].$$ (1.3)

~~We see~~ the particle's velocity exponentially decays with rate ζ/m from its initial value to a steady state value f/ζ. Now, if we ~~can only make measurements at or~~ are interested in time scales larger than m/ζ, the velocity is ~~always~~ constant. Brownian dynamics is this overdamped limit: the velocity decays so quickly to a steady state value that we can drop the inertial terms from the Langevin equation.

In the overdamped limit, the Langevin equation describing Brownian dynamics [16, 26],

$$\dot{x} = -\zeta^{-1}\left[-\frac{dU}{dx} + \xi(t)\right].$$

(1.4)

~~Upon examining~~ Eqn. 1.4 ~~further, we will show how it~~ resembles a random walk ~~and~~ discover the connection between the Langevin equation and diffusion.

1.2   Random walks 101

~~Given~~ the random fluctuating force~~, it is not surprising that there~~ is a connection between Brownian dynamics and a discrete random walk. By discrete, I mean that the particle will take a random step Δx and a rate $1/\tau$. On average, $\langle\Delta x\rangle = 0$ and $\langle\Delta x^2\rangle = l^2$. After N steps, its total displacement is a sum over i steps

$$x_N - x_0 = \sum_i^N \Delta x_i.$$

(1.5)

This equation is at the heart of the lattice Monte Carlo models and BD simulations we will discuss later~~; a particle undergoes a random walk in which moves of determined by the rolling of a die.~~ Let's imagine repeating this experiment several times. In doing so, we hope to say something meaningful about the average behavior of the motion by exploiting the properties of the random step. Upon averaging over experiments, the mean square displacement is

$$\langle x_N - x_0\rangle^2 = \left\langle\sum_i^N \Delta x_i \sum_j^N \Delta x_j\right\rangle = Nl^2 = 2Dt,$$

(1.6)

where $D = \frac{l^2}{2\tau}$. Here, we used the fact that steps at different times are uncorrelated $\langle\Delta x_i\Delta x_j\rangle = \delta_{ij}l^2$ and that $N = \frac{t}{\tau}$ where t is the total time of the random walk. D is the diffusion coefficient;

it connects the measurable spread of a random walk, $i.e.$ $\langle x^2 \rangle$, to time. For arbitrary dimension d, the MSD is

$$\langle r^2(t) \rangle = 2dDt, \tag{1.7}$$

where now $D = \frac{l^2}{2d\tau}$ and τ is the step frequency along any dimension.

A brief comment on what we mean by averaging $\langle ... \rangle$. Typically—and in this paper—this is called an ensemble or noise average. This means repeating the experiment with the same initial conditions and averaging the results. By doing this, we are exploiting the average properties of the noise.

Now that we explained the connection between random walks and the diffusion coefficient, we can return to Eqn. 1.4 ~~to see where Brownian dynamics fits into the story~~. In the absence of interactions and fields, the overdamped Langevin equation is

$$\dot{x} = \zeta^{-1}\xi(t). \tag{1.8}$$

Upon integration with respect to time, we get

$$x(t) - x(0) = \int_0^t \zeta^{-1}\xi(t')dt'. \tag{1.9}$$

Since ξ is a random force, we can interpret this integral as a sum of random steps of length $\zeta^{-1}\xi(t')dt'$ [26].

~~Upon a closer inspection of Eqn. 1.9, we can tease out a connection to the diffusion coefficient.~~ Let's write the integral as a sum over N_t time steps of length δt—$i.e.$ $t = \sum_i^{N_t} \delta t$. This discretization gives

$$x(t) - x(0) = \int_0^t \zeta^{-1}\xi(t')dt' \approx \sum_i^{N_t} \zeta^{-1}\xi_i \delta t. \tag{1.10}$$

When we discretize time, we are assuming that the noise is constant over the length of a time step. Since ξ is uncorrelated in time, we summing ~~up a bunch of~~ uncorrelated steps just like in the discrete random walk. We can also translate ξ into a time discretization framework, $\langle \xi_i \xi_j \rangle = \frac{2\zeta k_B T}{\delta t}\delta_{ij}$ [27]. Thus, the mean squared displacement can be written as

$$\langle (x(t) - x(0))^2 \rangle \approx \sum_i^{N_t}\sum_j^{N_t} \zeta^{-2}\langle \xi_j \xi_j \rangle \delta t^2 \approx= \frac{2k_B T \delta t}{\zeta}N_t = \frac{2k_B T}{\zeta}t. \tag{1.11}$$

Comparing ~~this to~~ Eqn. 1.11 to Eqn. 1.7, we see ~~that we have found~~ the Einstein relation [17],

$$D = \frac{k_B T}{\zeta}.$$ (1.12)

It is common to express the inverse friction as the mobility $\mu = \frac{1}{\zeta}$. I will mention the mobility throughout the thesis while avoiding ~~this notations~~ to avoid confusion with the chemical potential, also called μ. Eqn. 1.12 can be derive through other means [16, 26]~~, but I find this framework naturally connects to Brownian dynamic simulations because time discretization is precisely what is done in Brownian dynamic simulations.~~ Typically, we are looking at something a little more interesting—interacting particles, external fields, etc. Regardless, we imagine discretizing time and adding up small positional changes that occurred over a time interval [27]. ~~For those interested,~~ the basic methods behind Brownian dynamic simulations are summarized in Appx. B.

Finally, we ~~will~~ connect the Brownian dynamics to a continuity equation—*i.e.* instead of examining a single random walk, what can we say about the probability of finding the particle at a given location and time. Since a Brownian particle ~~is~~ undergoing a random walk, its position is ~~given by~~ a sum of independent random variables. By the central limit theorem, the distribution of positions must Gaussian [26]. ~~We also know that our~~ variance along any given dimension i must be $\sigma_i^2 = \langle x_i^2(t) \rangle = 2Dt$. Thus, the probability density in d dimensions is

$$p(\boldsymbol{r}, t) = \frac{1}{(4\pi dDt)^{d/2}} e^{-\frac{\sum_i^d x_i^2}{4Dt}}.$$ (1.13)

Here, we have assumed that the particle has started at origin— ~~take~~ the $t \to 0$ limit ~~to see we~~ recover a delta function centered at the origin. ~~By taking derivations of this distribution with respect to time and space, we can verify that~~ this distribution obeys the diffusion equation

$$\frac{\partial p(\boldsymbol{r}, t)}{\partial t} = D\boldsymbol{\nabla}^2 p(\boldsymbol{r}, t).$$ (1.14)

~~Most of the time,~~ we are interested in tracking ~~a concentration of~~ noninteracting Brownian particles. The single-particle probability distribution and concentration ~~just~~ differ by a factor of the particle number N since there are no correlations between particles. We can therefore write the diffusion

equation as~~,~~

$$\frac{\partial c(\boldsymbol{r},t)}{\partial t} = \boldsymbol{\nabla} \cdot \boldsymbol{j}_{\text{diff}} = \boldsymbol{\nabla} \cdot D\boldsymbol{\nabla}c(\boldsymbol{r},t). \tag{1.15}$$

From this, we can extract ~~the~~ Fick's law of diffusion [26]

$$\boldsymbol{j}_{\text{diff}} = D\boldsymbol{\nabla}c(\boldsymbol{r},t). \tag{1.16}$$

The diffusion coefficient is a constant scalar in our derivation because we assumed that the friction coefficient is isotropic and homogeneous. ~~In general, it may not be.~~

~~Taking a step back, we can review what was covered and its connection to the research presented in this thesis. Starting from the Langevin equation, we discussed the overdamped limit in which we recovered Brownian dynamics. We connected the drag and diffusion coefficient, through the Einstein relation, which illuminated how Langevin equation relates to discrete random walks. We touched on how discrete random walks and the Langevin equation are connected the lattice Monte Carlo models and Brownian dynamic simulations. We concluded by connecting the microscopic dynamics to a continuity equation of the concentration.~~

From here, we ~~will~~ briefly introduce ~~what happens when we introduce~~ obstacles and interactions ~~into the picture. This will set the stage for some specific systems covered in this thesis. These will all be discussed in more detail in the further chapters, but it helps to introduce the bigger picture here.~~

1.3 Effects of obstacles

~~We have just spent some effort understanding the core picture of BD simulations: the random walk.~~ While random walks are useful for describing dynamics of particle in many situations, it is ~~far from the whole story in physical systems~~. Particle dynamics can by altered from interactions with either other particles or the environment. In crowded media, obstacles impede tracer motion—*e.g.*, diffusion of macromolecules in a cell [2]. A profound effect of these obstacles is that the random walk can become anomalous [28].

One of the key assumptions in a normal random walk is that steps are attempted at a constant frequency. When this occurs, the MSD is linear in time (Eqn. 1.7)—referred to as Fickian or normal diffusion. If this assumption is relaxed and the MSD is no longer linear in time [28],

$$\langle r^2 \rangle = 2dDt^\alpha, \tag{1.17}$$

and the diffusion is anomalous. ~~An~~ inhomogeneous scattering of obstacles can impede motion ~~of a particle~~ and cause ~~an~~ variable step frequency [29, 30]. In ~~several~~ biological system, anomalous diffusion has been measured due to the presence of obstacles [31–33]. Since the early work of Saxton [34], lattice Monte Carlo models have been an important tool for studying diffusion in crowded environments. Obstacles ~~are represented as energy landscapes which~~ affect the probability to move to a certain location.

While there are myriad models [30,34–43], ~~one important model missing was one that included~~ bound motion and soft obstacles. There are several biological systems that suggest bound motion and soft—*i.e.*, particles and obstacles can occupy the same spatial region—obstacles [44–48]. The model we developed in [21] studied how bound motion and binding affect tracer dynamics.

Another type of obstacle ~~that can be imagined~~ is a homogeneously distribution of binding sites which a particle can attach to. The binding is controlled by ~~some~~ binding kinetics

$$T + B \rightleftharpoons C, \tag{1.18}$$

where T is the concentration of unbound particles, B is the concentration of binding sites, and C is the concentration of the bound complex. ~~While diffusing,~~ a particle could bind to the uniform background of binding sites which alter its motion. This was the model we developed to understand how biofilters, ~~namely the nuclear pore complex,~~ select which particles are allowed to pass through [49].

1.4 Effects of interactions and activity

Active matter is collections of interacting particles which are propelled by a nonconservative force. ~~It is a~~ novel system ~~that~~ illuminates how particle interactions and activity can lead to

~~unique~~ properties—such a giant number fluctuations and unusual mechanical responses [15]—that

~~not~~ present in equilibrium systems. We are interested in how microscopic interactions lead to

bulk behavior. Introducing interactions and activity to the Langevin equation is ~~a~~ straightforward

~~process~~. In a simulation, one can image calculating ~~some~~ forces on each particle ~~and~~ updating

~~the~~ positions ~~in a simulation~~, and analyzing the results. ~~That~~ simulation, however, was just one

possible outcome—*i.e.*, one realization of the noise. ~~One may wonder if the behavior was simply~~

~~'by chance'. If we'd like~~ to say something about the average behavior, we would have to repeat

the simulation many times. Another method~~—which I will refer to as a continuity, continuous, or~~

~~macroscopic equations—~~would be evolve a probability density in time, like in the diffusion equation

(Eqn. 1.15). ~~Both simulations and continuity equations have their advantages and disadvantages~~

~~which I hope to illuminate below.~~

When evolving the Langevin equation, the corresponding microscopic density of a system of
point-like particles is [50]

$$\hat{\rho}(\boldsymbol{r}) = \sum_{i=1}^{N} \delta(\boldsymbol{r} - \boldsymbol{r}_i). \tag{1.19}$$

~~A particle is either at a location or it isn't.~~ This density is an operator since it is only truly

meaningful in an integral. ~~What we are interested in is an~~ ensemble averaged density ~~which could~~

~~tell us~~ how the system behaves after ~~we~~ average over ~~all~~ noise ~~realizations~~,

$$\rho^{(1)}(\boldsymbol{r}) = \langle \hat{\rho}(\boldsymbol{r}) \rangle = \left\langle \sum_{i=1}^{N} \delta(\boldsymbol{r} - \boldsymbol{r}_i) \right\rangle, \tag{1.20}$$

where $\rho^{(1)}(\boldsymbol{r})$ is the one-body density. Typically, the (1) superscript is dropped or ~~it's~~ denoted as

~~$\rho(\boldsymbol{r})$ or~~ $c(\boldsymbol{r})$, and ~~it~~ is also referred to as density profile or concentration. The one-body density

the noise ensemble average probability of finding a particle at location $\boldsymbol{r}$. ~~Here, we can already~~

~~see a few advantages of~~ solving continuous equations ~~over simulation. First, we just need~~ to evolve

the dynamics at spatial coordinates instead of for ~~the~~ N particles. As N ~~gets large~~, the BD

numerics becomes unwieldy. ~~For larger particle number, solving continuous equations becomes a~~

~~much more realistic numeric approach. Also, we gain insight on the general behavior of a system.~~

~~We have already seen an example of the temporal evolution of this density: the diffusion equation~~

(Eqn. 1.15). ~~While we have no idea a priori what will exactly happen during a simulation, we expect that the particles are going to spread out. This is precisely what Eqn. 1.15 describes.~~

A technique for solving the temporal evolution of density is dynamical density functional theory (DDFT) [22–25]. Using DDFT, a continuity equation for the evolution of the one-body density is expressed in terms of functional derivatives of the free energy $\mathcal{F}$

$$\frac{\partial \rho(\boldsymbol{r}, \boldsymbol{t})}{\partial t} = -\boldsymbol{\nabla} \cdot \boldsymbol{j} = \boldsymbol{\nabla} \cdot \left[\zeta^{-1} \rho(\boldsymbol{r}, t) \boldsymbol{\nabla} \frac{\delta \mathcal{F}\left[\rho(\boldsymbol{r}, t)\right]}{\delta \rho(\boldsymbol{r}, t)} \right]. \tag{1.21}$$

We can interpret the flux $\boldsymbol{j} = \rho \boldsymbol{v}$ as a concentration, ρ, times a velocity $\boldsymbol{v} = -\zeta^{-1} \boldsymbol{\nabla} \frac{\delta \mathcal{F}[\rho]}{\delta \rho(\boldsymbol{r})}$. The velocity term arises from the gradients of ~~a~~ chemical potential $\mu(\boldsymbol{r}) = \frac{\delta \mathcal{F}[\rho]}{\delta \rho(\boldsymbol{r})}$.

The nonconservative active force cannot be expressed as a gradient of a chemical potential. However, it can described by an active flux $\boldsymbol{j}^{\mathrm{act}} = \rho(\boldsymbol{r}, t) \boldsymbol{v}^{\mathrm{act}}$. Our total flux will therefore be given by

$$\boldsymbol{j} = \boldsymbol{j}^{\mathrm{DDFT}} + \boldsymbol{j}^{\mathrm{act}}. \tag{1.22}$$

~~One final comment on the free energy functional in Eqn. 1.21 is that~~ we can ~~always~~ separate the free energy into contributions from ideal gas entropy $\mathcal{F}^{\mathrm{id}}$, interactions or excess $\mathcal{F}^{\mathrm{ex}}$, and external fields $\mathcal{F}^{\mathrm{ext}}$ [50],

$$\mathcal{F} = \mathcal{F}^{id} + \mathcal{F}^{ex} + \mathcal{F}^{ext}. \tag{1.23}$$

The ideal gas and external fields contribution are known exactly. The crux of DDFT is approximating a functional for the interactions~~, which in general is unknown~~ [25].

In this thesis, I will describe how the DDFT framework can be used to solve for the temporal evolution of active systems. I will then apply it a self-propelled hard needle system [51–56]. I will present novel results including a banding instability and discuss where my work fits into the larger body of work [57].

Chapter 2

Soft sticky and slippery obstacles

The diffusion of macromolecules in crowded environments is generally slowed relative to the uncrowded case, and particle motion can undergo transient anomalous subdiffusion [2]. The motion of lipids or macromolecules within biological membranes can be affected by crowding [3–10] because the membrane contains both macromolecules and inhomogeneities in membrane composition [58,59]. In the cell interior, macromolecules, organelles and other cellular structures can inhibit motion, or in contrast, enhance sampling of non-crowded regions [11]. Biological crowders can also contain interaction sites which further modify the macromolecular motion [60]. The kinetics and equilibrium behavior of interactions between mobile proteins can be modified by crowding [61,62]. The magnitude of the effects of crowding on macromolecular motion and reactions is important to determine the limiting rate of biological processes such as signaling receptor activation.

Although most theoretical work has focused on anomalous diffusion in crowded systems made up of impenetrable obstacles with attractive or repulsive surfaces [30, 34–36, 40], there is growing evidence of the importance of soft compartments and barriers in biological systems. In membranes, lipids may be only partially excluded from lipid rafts or domains. When they do interact, they can still diffuse within them [63–66]. Lipid motion can be hindered, though not stopped, near α-synuclein protein aggregates [67]. For all of these cases, theoretical considerations of a two-dimensional system should include the effects of soft interaction potentials and bound-state mobility.

Inside the cell, intrinsically disordered or low-complexity domains can act as soft obstacles or

wells, with rapid diffusion within the wells. Membraneless organelles spontaneously form from low-complexity domain proteins. They are typically highly dynamic assemblies [44], which show fast intra-particle diffusion times, and allow rapid entry and exit of constituents [45]. Proteins which interact with intrinsically disordered proteins can still diffuse during the binding interaction [46, 47]. This effect may be particularly pronounced in the central channel of the nuclear pore complex, which contains a high density of binding sites on intrinsically disordered domains. Recent simulation work suggests that the disordered protein binding pockets can exchange on transport factors [47], providing a clear mechanism for mobility while bound to an obstacle. Particles are weakly excluded from individual disordered protein chains due to the lowering of the polymer chain entropy [48], but are expected to allow other macromolecules to enter, and pass through, the space that they occupy. The increasingly recognized importance of proteins which are intrinsically disordered or contain low-complexity domains within their assemblies warrants a more careful consideration of the differences between the previously well-studied models, in which binding immobilizes the bound species, and a model which includes soft interactions and obstacles or barriers in which the bound species may remain mobile.

Motivated by the biological importance of binding interactions which can retain mobility of the bound particle, we studied a minimal model with bound tracer mobility (Figure 2.1). In our model, tracer particles move on a 2D or 3D lattice in the presence of immobile obstacles, to which the tracers can bind. A primary distinction between our model and many others that consider binding or adhesion is that others typically consider adhesion between a tracer and an adjacent hard obstacle, in which there is no overlap between tracers and a hard obstacles core [35, 40, 43]. Here, obstacles are soft: tracer particles can overlap with obstacles, with an energy penalty (or gain) ΔG upon moving to a lattice site occupied by an obstacle. Unlike previous work modeling lipid rafts, we closely examine the dependence on binding, instead of just pure exclusion or free entry into lipid regions [5].

To understand the effects of bound mobililty, we first consider the limits of 'sticky obstacles', in which tracers are immobile while bound, and 'slippery obstacles', in which tracers are mobile

while bound. We use lattice Monte Carlo methods to explore a range binding energy and obstacle filling fraction. We also examine the effects of semi-sticky obstacles—*i.e.,* intermediate bound diffusion coefficient—and obstacle size effects. Our work demonstrates how diffusion is altered in a crowded environment with compartments with different properties—such as a cell [68]. Our results demonstrate how binding and bound-state motion independently impact particle dynamics, including long-time normal diffusion and anomalous diffusion. Bound tracer mobility increases the long-time diffusion coefficient, reduces the transient anomalous time, and eliminates caging for all times typically observed above the percolation threshold. These results demonstrate that mobility of bound particles can benefit biological systems by allowing mobility even in highly crowded environments.

2.1 ~~Basic~~ anomalous diffusion ~~theory~~

Fractional or anomalous diffusion has been experimentally measured in cells, using fluorescence recovery after photobleaching [31], fluorescence correlation spectroscopy [32, 69], and single-particle tracking [33]. Anomalous diffusion in crowed environments is typically described by a MSD that is no longer constant in time [28]

$$\langle r^2 \rangle \sim t^\alpha, \tag{2.1}$$

where α is called the anomalous coefficient. The magnitude of α describes the type of diffusion ~~present~~: subdiffusion ($\alpha < 1$), Fickian ($\alpha = 0$), and superdiffusion ($\alpha > 1$). ~~It should be mentioned that~~ there is a ~~corresponding~~ fractional diffusion equation associated with the dyanmics in Eqn. 2.1, but we will neglect discussing it further ~~as it is not important for our purposes~~—see [28, 29] for more details.

~~An underlying assumption of~~ a traditional Fickian random walk ~~is that~~ the step rate occurs at a fixed interval. In a continuous-time random walk, this assumption is relaxed. ~~Instead,~~ the waiting-time before taking a step is sample from a distribution. A continuous-time random in which the mean waiting time diverges—*e.g.,* with a power law waiting-time distribution—results

in anomalous diffusion [28, 29].

An inhomogeneous arrangement of hard obstacles can provide an irregular step rate which can introduce memory effects into the system [29]. One way of viewing viewing anomalous diffusion the presence of obstacles is by considering the fractal structure of obstacle cluster [30, 34]. Clusters of random hard objects are fractal over short length scales and homogeneous over larger length scales. On length scales larger than the fractal structure, for which the landscape is homogeneous, the diffusion becomes normal ($\alpha = 1$). The Fickian diffusion constant again when $\alpha = 1$ is just a measure of the long time behavior of a tracer diffusing in this homogeneous environment. $\alpha \neq 1$ occurs over when considering the dynamics of a diffusing for length scales in which clusters of hard obstacles are fractal [34].

α can be therefore thought of a measure of non-homogeneity and fractal structure of a local landscape. It does not directly describe the time it takes to escape an trapping cage; just that there is a possibility that the landscape could trap a tracer. In $\alpha \to 0$ limit, a tracer is fully caged, and $\alpha \to 1$ is Fickian diffusion, albeit with a lower step rate than free diffusion. We will refer to t_a informally as the anomalous time and provide a more rigorous definition in the Model section. Qualitatively, it is the crossover time from short time subdiffusion to long time Fickian diffusion. We can think of α as a measure of how trapped a tracer; t_a describes how long it takes a tracer to escape a cage it was in and forget the memory effects that cage introduce in its motion. Just as with standard random walks, we really only measure things in terms of an ensemble average. Similarly, if there is nothing that explicitly breaks time translation, e.g., a field that is turned on for a certain time, all of our measurements can be averaged of time intervals $\Delta t = t_1 - t_2$. Thus, t_a describes a time scale, irrespective of a particular clock.

2.2   Lattice models

Lattice Monte Carlo is an indispensable tool for studying diffusion in crowed media. The basic principle is that a tracer particle undergoes a random walk on a lattice. There are obstacles present on the lattice that can alter dynamics of the tracer by inhibiting steps, lowering the step

attempt rate, etc. The typical procedure is at a given time step a random number is generated. Based on that number, a particle will attempt a step in a given direction. If there are obstacles present, a move will be accepted or rejected based on the interaction with that obstacle. For example, is an obstacle is impenetrable and a tracer tries to step there, the move is rejected. We can also image obstacles effect the local energy landscape. If there is an energy difference ΔE associated with moving between lattice sites, moves are accepted with a probability based on the Boltzmann factor $P_{\text{accept}} \sim e^{-\beta \Delta E}$. ~~With the fundamentals in place, we can examine some previous results in the field and comment on how our model expands on them~~.

Our model seeks to build on stochastic lattice-gas models that have been important to understanding tracer dynamics in the presence of immobile and mobile hard obstacles [34], anomalous subdiffusion [30], and effects of binding on diffusion [35]. Saxton showed that the tracer diffusion coefficient drops to zero at the percolation threshold, the critical concentration of obstacles at which a continuous path of vacancies through which a tracer can move, no longer exists. Above this percolation threshold, diffusion is anomalous at long time. The effects of tracer and obstacle size [36, 38, 39] and adhesion and repulsion to sites adjacent to obstacles [40] on transient subdiffusion and long-time diffusion have been studied. Extensions to mobile obstacles which interact with each other have demonstrated how obstacle clustering dynamics can influence the diffusivity of tracers [70].

Numerically exact methods for calculating diffusion coefficients using the Nernst-Einstein relation [71, 72] and Markov chains [37] have been implemented as a different approach to analyzing these systems; the Nernst-Einstein approach can lower the computational cost of measuring diffusion coefficients for lattice gases [39]. Protein motion in polymer networks has been studied using random-walk and self-avoiding-chain models for immobile [42] and mobile [43, 73] hard chains. Studies of chains with binding sites found that modeling chain dynamics allowed a mapping onto randomly distributed obstacles with an effective volume, and showed how sliding along a defined chain can effect tracer dynamics [41, 73]. In some previous work, the effects of binding and sliding while bound were entangled because both effects were encoded by a single parameter [41, 73]. Do-

mains with different diffusion coefficients and sizes—to model lipid rafts—have been studied, but the analysis only included total or no exclusion although it was noted that binding effects could play a large role [5].

2.3   Model

In our model, tracer particles undergo a random walk on a square lattice and interact with immobile obstacles. The interaction is characterized by a binding free energy; for simplicity, we neglect any additional activation barrier. The characteristic binding free energy change of a tracer that hops from an empty site to an obstacle site is ΔG (in units where $k_B T = 1$). We consider both attractive ($\Delta G < 0$) and repulsive ($\Delta G > 0$) obstacles. We use the Metropolis algorithm [74] to accept or reject candidate binding (probability P_B) and unbinding (probability P_U) events. Each tracer occupies a single site lattice site, but the obstacle size is varied to represent domains of characteristic size. Obstacles are squares with sides of length l_{obst}, measured in units of the lattice spacing.

To study the effects of tracer particle motion while bound, we considered the limits of perfectly sticky and slippery obstacles Figure 2.1, as well as the intermediate 'semi-slippery' case. In all models, obstacles are soft, so that tracers overlap with obstacles when bound. For sticky obstacles, no hopping between obstacle sites can occur, but tracers can exit an obstacle to an unoccupied site. For slippery obstacles, tracers can hop between adjoining obstacles while remaining bound. In the limit of perfectly slippery obstacles, bound motion is identical to unbound motion: there is no difference in hopping rates between free and bound tracers. For semi-slippery obstacles, we vary the bound diffusion coefficient.

2.3.1   Simulation methods

In our kinetic Monte Carlo scheme, at each time step a tracer attempts a move in a randomly chosen direction. Moves from **empty** $\rightarrow$ **empty** are always accepted, **empty** $\rightarrow$ **obstacle** moves are accepted with probability $P_B = \min(e^{-\Delta G}, 1)$, **obstacle** $\rightarrow$ **empty** moves are accepted with

probability $P_U = \min(e^{\Delta G}, 1)$, and **obstacle → obstacle** moves are always accepted/rejected if obstacles are slippery/sticky (Figure 2.1); for semi-slippery obstacles, the acceptance probability is $D_{\text{bound}}/D_{\text{free}}$. If a tracer's move is rejected, it remains immobile for that time step. We assume noninteracting tracers.

Initially, obstacles were uniformly randomly placed on the lattice, at the specified filling fraction, without overlaps. Next, tracers were randomly placed on obstacles and empty sites at their equilibrium occupancy, as determined by the filling fraction of obstacles ν, and binding energy ΔG. The fraction of tracers on obstacles is proportional to the obstacle filling fraction times the Boltzmann factor $\nu e^{-\Delta G}$, while the fraction of tracers on empty sites is proportional to the fraction of empty sites $(1 - \nu)$. The equilibrium fraction of tracers on obstacles of size one is then

$$f_o = \frac{\nu e^{-\Delta G}}{\nu e^{-\Delta G} + (1 - \nu)}. \tag{2.2}$$

Using an initial fraction of tracers bound to obstacles determined from f_o avoids the time required for binding equilibration in the simulations, ensuring that mean-squared displacement measurements are independent of a time origin.

We performed 2D simulations with 200 tracers on a 256×256 periodic lattice for $10^5 - 10^{7.5}$ time steps, with a recording interval of $10 - 100$ steps. For each parameter set (determined by filling fraction and binding energy), we averaged over 96 separate obstacle configurations. We varied ν from 0 to 1 and ΔG from -5 to 10. Three dimensional simulations used similar parameters with a $256 \times 256 \times 256$ periodic lattice. In the semi-slippery case, we varied the ratio of bound to free diffusion coefficient $D_{\text{bound}}/D_{\text{free}}$ between 0 (perfectly sticky) and 1 (perfectly slippery) in steps of 0.2, for binding energy $\Delta G = 1, 2, 3, \infty$ for filling fraction, $\nu = 0.3$ and 0.6. When varying obstacle size, we used square obstacles with the length of a side, l_{obst}, equal to odd values from 1 to 15. When varying obstacle size, we studied repulsive obstacles, to understand how binding affects diffusion for finite repulsion between the previously-studied free binding and pure exclusion limit [5,36]. ~~When varying obstacle size, we studied repulsive obstacles, to understand how binding affects diffusion for finite repulsion between the previously-studied free binding and pure exclusion~~

2.3.2   Trajectory analysis

We determined tracer mean-squared displacement (MSD) as a function of time delay by averaging over all tracers, 100 randomly selected independent time origins, and obstacle configuration. For long time delays for which 100 independent time intervals were not available, we averaged over the maximum number of independent time intervals. As previously mentioned, averaging over time windows improves our statistics; note that the time origins are not unique, since the placement of tracers in their equilibrium binding distribution ensures that there is no initial binding equilibration time. We have verified that that are no aging effects [75, 76], *i.e.*, MSD measurements that depend on simulation time, in our model (data not shown).

We sought to quantify the effects of binding and obstacle filling fraction on tracer mobility. In systems with either purely Fickian diffusion or particular obstacle geometry, the mean-squared displacement grows as a power law in time:

$$\langle r^2 \rangle = 2dDt^\alpha, \tag{2.3}$$

where $\langle r^2 \rangle$ is the ensemble-, time-origin-, and obstacle-configuration-averaged mean-squared displacement, d is the spatial dimension, D is the diffusion coefficient, α is the diffusion scaling exponent, and t is the time delay. This fractional diffusion equation has been studied extensively [28], both because it emerges from certain microscopic theories and as a means to quantify anomalous random walks. For hard obstacles, α reflects the non-homogeneity and fractal structure of a cluster. In this case, α can be thought of as a measure of a local landscape, in which obstacles have the possibility of trapping a tracer and introducing memory effects into the system. The value of α does not quantify the time it takes to escape a trapping cage; but $\alpha < 1$ suggests the possibility that the landscape can cage tracers. In the $\alpha \to 0$ limit, a tracer is fully caged, and the $\alpha \to 1$ limit represents Fickian diffusion.

However, many systems have more complex dynamics that are not power law. For example,

tracer dynamics can be transiently anomalous: subdiffusive on short time scales and Fickian on longer time scales (Figure 2.2b). The dynamics can be quantified using a phenomenological approximation in which the exponent α is treated as time dependent [30, 36–39, 77]. Thus, $r^2 \sim t^\alpha$ holds only over particular time scales.

For non-power-law dynamics, we can apply Eqn. 2.3 locally, with a phenomenological, time-varying exponent. Then $\alpha(t)$ is defined by local fitting to the logarithm of $\frac{\langle r^2 \rangle}{t}$:

$$\log \left(\frac{\langle r^2 \rangle}{t} \right) = \log \left(2dD \right) + \left(\alpha(t) - 1 \right) \log \left(t \right), \tag{2.4}$$

so that $\alpha(t) - 1$ is the local slope of the $\frac{\langle r^2 \rangle}{t}$ versus t curve on a log-log plot. As seen in figs. 2.2 and 2.3, the instantaneous effective α varies with delay time. Thus, a power-law MSD scaling with time, such as can arise from fractional Brownian dynamics, does not encompass the complexity of our crowded diffusion model, as has been found previously [9, 38].

In practice, we binned Eqn. 2.4 into separate regions of order 10. We locally fit the slope— we assumed a linear function —of each region. If it was below a certain threshold value, we assumed it was flat. We then took a weighted averaged all points from that bin on to get the horizontal asymptote. α was found from the maximum slope of these bins, and t_a was calculated from the intercept of the horizontal asymptote and the fit line from the bin associated with α.

At short time, our model typically exhibits anomalous diffusion. However, in some conditions, the short-time behavior is diffusive, with an intermediate anomalous regime. We defined $\alpha_{\min}$ as the minimum instantaneous value of α (the most anomalous exponent). We characterized the transition between short- or intermediate-time anomalous diffusion and long-time normal diffusion by the time scale t_a, determined as the intersection of the horizontal long-time asymptote of $\frac{\langle r^2 \rangle}{t}$ with a line tangent to the point of the maximum rate of decrease of this curve (Figure 2.3b,c). We found that this transition time could be robustly determined for a wide range of diffusion coefficients and anomalous behavior. We denote t_a the anomalous time. Qualitatively, it is the crossover time from short-time subdiffusion to long-time Fickian diffusion. While $\alpha_{\min}$ characterizes how trapped a tracer is, t_a quantifies how long it takes a tracer to escape a cage.

We defined the long-time Fickian diffusion coefficient as

$$D = \lim_{t \to \infty} \frac{\langle r^2 \rangle}{2dt}. \tag{2.5}$$

All diffusion coefficient measurements are expressed in terms of the scaled diffusion coefficient $D^* = \frac{D}{D_0}$, where $D_0 = \frac{l^2}{2d\tau}$ is the diffusion coefficient in the absence of obstacles, ~~where~~ l ~~is~~ the distance between lattice sites (here defined to be 1), and τ the time interval between steps (also set to 1).

In some cases, we were unable to determine all of D^*, $\alpha_{\min}$, and t_a. For some parameter sets, the slope of $\langle \frac{r^2}{t} \rangle$ vs. t on a log-log plot approached a non-zero constant, indicating that diffusion was anomalous over all measured time delays, so that the Fickian diffusion coefficient was not well-defined. For other parameter sets, the $\langle \frac{r^2}{t} \rangle$ versus t curve did not reached a clear asymptote during the simulation time. We therefore could not determine D^*, but could measure $\alpha_{\min}$. When tracer diffusion was normal over all or nearly all measured time delays, neither $\alpha_{\min}$ nor t_a were well-defined, but D^* could be measured.

2.4   Sticky soft obstacles

We initially focus on the limit of perfectly sticky obstacles of size 1, to determine the effects of stickiness, filling fraction, and binding energy on tracer motion. We varied parameters over a wider range for the 2D model, with a comparison to 3D results for some parameter sets.

For sticky obstacles, the motion of a bound tracer to an adjacent obstacle is prohibited. This could occur, for example, because the net free energy cost of binding to an obstacle is a result of an attractive binding interaction, with a high free energy barrier to moving to an adjacent site. Here, we consider the limit that the free energy cost of moving to an adjacent obstacle is so large that it approaches infinity. This situation provides an important point of comparison to explicitly test the effects of bound-state diffusion on tracer behavior.

We separately consider repulsive and attractive obstacles (Figure 2.4). Note that we include the case $\Delta G = 0$, that is, where the binding interactions are neither attractive nor repulsive, but still

Figure 2.1: Model schematic. Tracers (colored circles) hop on a lattice of empty sites (white squares) and obstacles (gray squares). Tracer binding with a soft interaction potential allows them overlap with obstacles (top). For sticky obstacles, the only allowed moves of a bound tracer are to empty sites (unbinding). For slippery obstacles, tracers can hop to other obstacles while remaining bound. Arrows denote possible moves and P the probability that a given move is accepted.

Sticky obstacles:
no diffusion while bound.

Slippery obstacles:
diffusion while bound.
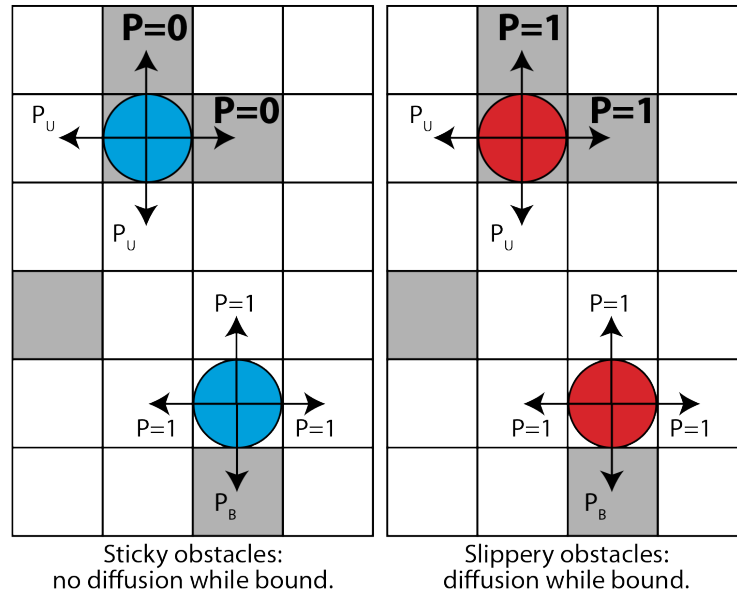
Figure 2.2: Mean-squared displacement $\langle r^2 \rangle$ divided by time delay t as a function of time delay t for (a) impenetrable obstacles, (b) repulsive slippery obstacles ($\Delta G = 2$), (c) repulsive sticky obstacles ($\Delta G = 2$), and (d) attractive sticky obstacles ($\Delta G = -2$). Different colors correspond to different filling fraction ν. Curves with non-zero slope indicate anomalous diffusion, and the horizontal asymptote indicates the long-time diffusion coefficient. Each curve represents an average over tracers, independent time windows, and obstacle configurations.
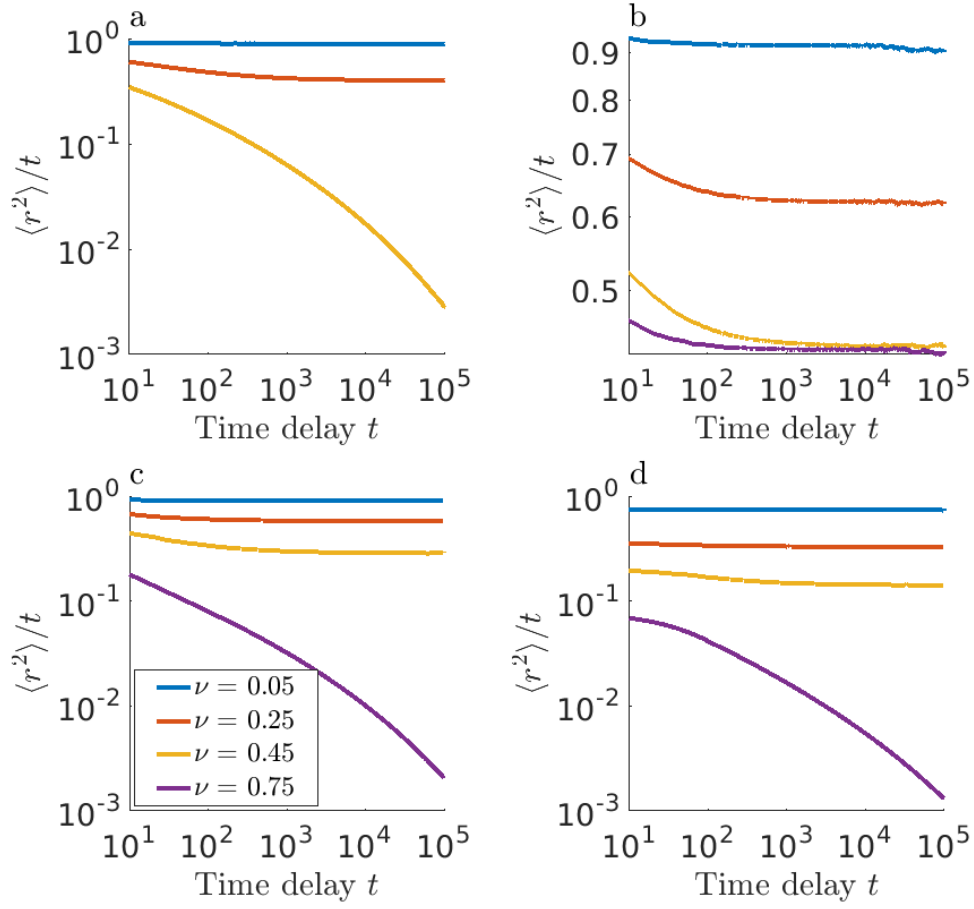
Figure 2.3: Top panel: Illustration of fitting procedure, showing $\langle r^2 \rangle / t$ vs time delay t for simulation data (blue), line fitted to horizontal asymptote (red dashes), line tangent to point of maximum absolute slope of the curve (red dash-dots), and anomalous time t_a (black dots) for different parameters. Bottom panel: instantaneous scaling exponent α vs time delay t. (a, d) Slippery obstacles with $\Delta G = 1$, $\nu = 0.95$: normal diffusion occurs for all measured time. (b, e) Sticky obstacles with $\Delta G = 2$, $\nu = 0.45$. (c, f) Sticky obstacles with $\Delta G = -5$, $\nu = 0.50$.

Figure 2.4: Sticky obstacles of size one in 2D. (a, d) Diffusion coefficient D^*, (b, e) anomalous time t_a, and (c, f) minimum scaling exponent $\alpha_{\min}$ as a function of obstacle filling fraction ν for repulsive (top) and attractive (lower) binding energy. Note that points for $\Delta G = 10$ are partially hidden behind $\Delta G = \infty$. The approximate locations of the critical occupancies ν^l and ν^u are indicated with gray dotted lines.
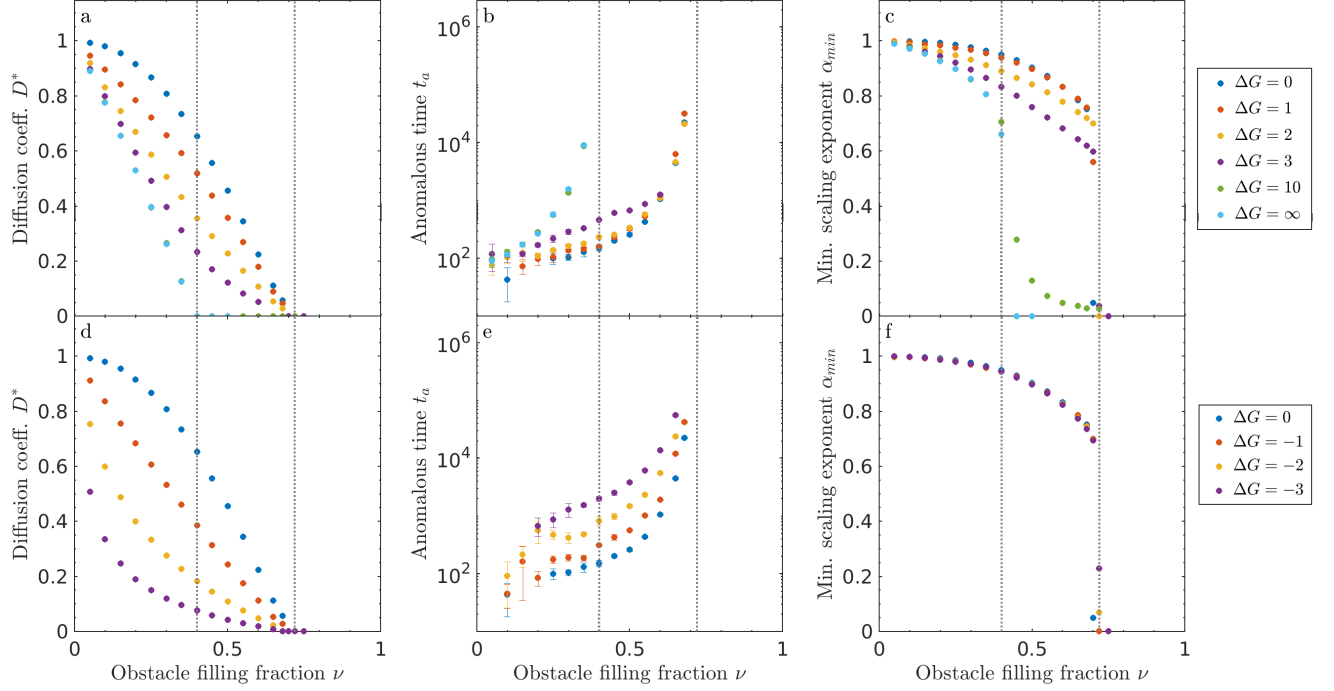
Figure 2.5: The two types of percolation threshold in our lattice model: the lower critical occupancy ν^l (left) and the upper critical occupancy ν^u (right). For the lower critical occupancy, which is the standard percolation threshold, the percolating network is the obstacles. At the upper critical occupancy, the percolating network is the *interface* between two or more obstacles. The barrier to tracer motion is shown as a black line; obstacle-obstacle boundaries which cannot be crossed by a tracer in the sticky model are shown in red. Without binding, tracers cannot pass through the percolating network of obstacles. If they can bind, tracers can 'hop through' a single obstacle, with or without bound motion.

Lower critical occupancy   Upper critical occupancy
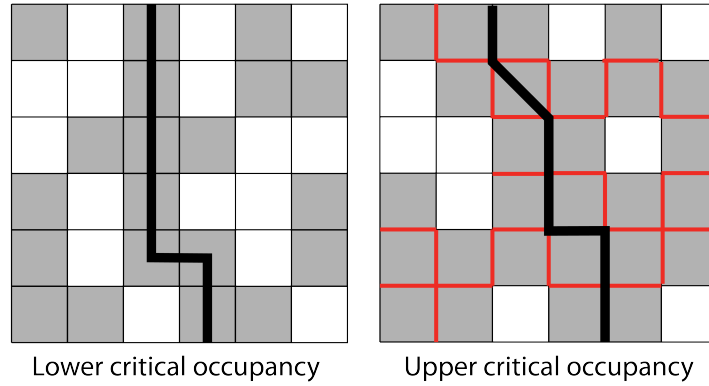
block moves to adjacent obstacles. We define the lower critical occupancy ν^l as the filling fraction at which ~~the~~ diffusion is non-Fickian for all time scales for impenetrable obstacles ($\Delta G = \infty$). In the limit of a hard repulsive obstacle, D^* decreases with filling fraction, and approaches zero at the percolation threshold expected for hard obstacles on a square lattice, $\nu^l \approx 0.4$ [78], where t_a diverges [34]. The lower critical occupancy is the percolation threshold, at which there is no longer a continuous path of empty sites (Figure 2.5).
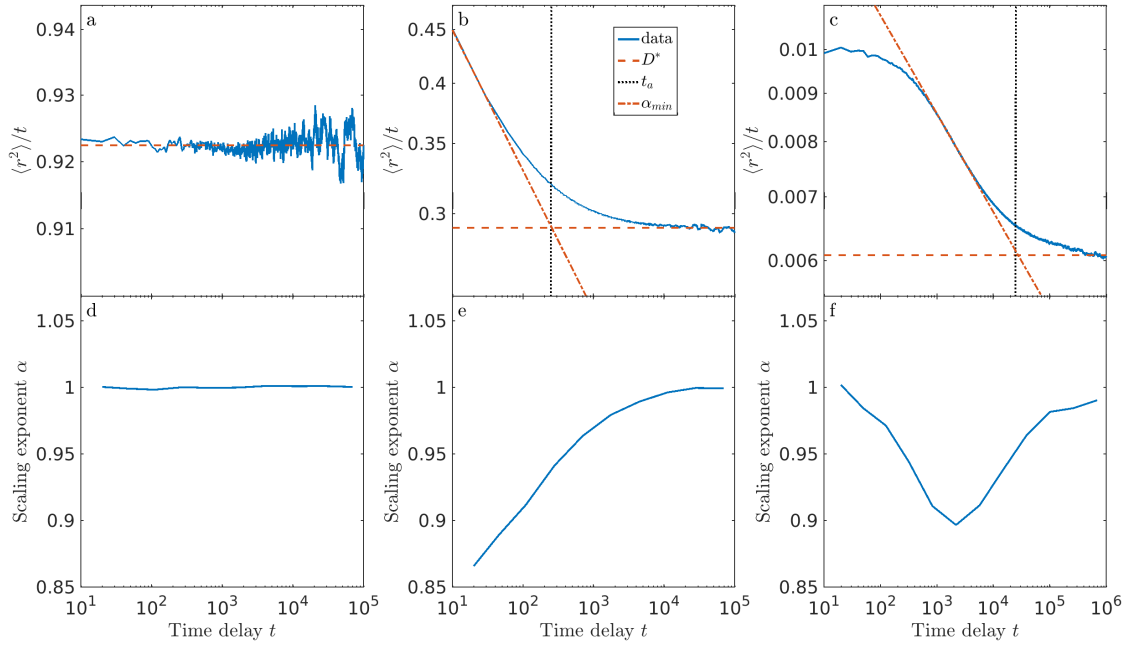
Figure 2.6: Sticky obstacles of size one in 3D. (a) Diffusion coefficient D^*, (b) anomalous time t_a, and (c) minimum scaling exponent $\alpha_{\min}$ as a function of obstacle filling fraction. The approximate locations of the critical occupancies ν^l and ν^u are indicated with gray dotted lines.

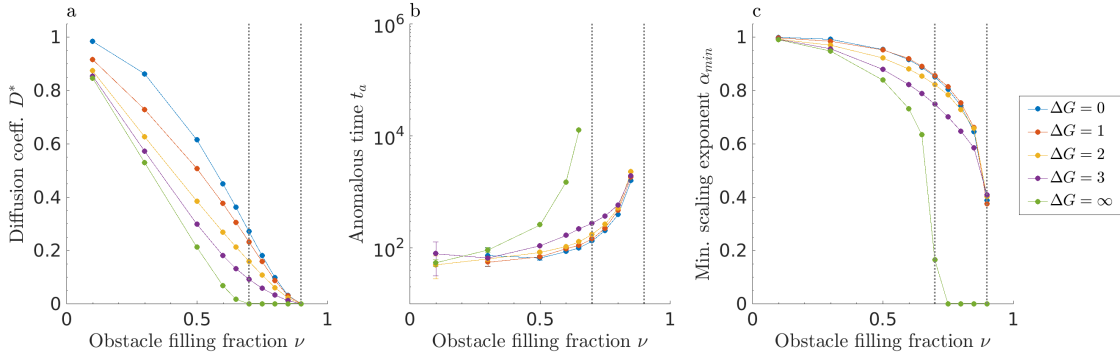For finite binding free energy in our model, Fickian diffusion can still occur above the percolation threshold ν^l because soft binding allows tracers to 'hop through' single obstacles via binding and unbinding. Without soft binding of the type we consider, obstacle percolation would prevent a tracer from moving between vacancy clusters. In other words, tracers that start in an area caged by obstacles are stuck there. With soft binding, tracers that start in a cage can hop onto an obstacle and then hop off into a new vacancy cluster. For soft binding interactions and sticky obstacles, there is an upper critical occupancy $\nu^u \approx 0.72$ at which the long-time diffusion coefficient approaches zero irrespective of binding energy (Figure 2.4). Above ν^u, tracers become caged regardless of the binding kinetics. Therefore, there is a different type of percolating network above the upper critical occupancy: the percolation of the inter-obstacle boundary (Figure 2.5). At the upper critical occupancy, there is a second adjacent obstacle preventing the tracer from 'hopping through.' Note

that as expected, the transition time t_a appears to diverge on the approach to the upper critical occupancy (Figure 2.4). We are unaware of a theoretical value for this percolating density, but our results suggest its approximate value is 0.72 in 2D (Figure 2.4).

Intermediate repulsive binding energy leads to intermediate behavior, as expected. For strong repulsion, *e.g.*, $\Delta G = 5$, D^* remains small, though clearly non-zero, up to the upper critical occupancy, while t_a monotonically increases until it diverges at ν^u.

Anomalous dynamics appear in the slope of $\langle r^2 \rangle / t$ on a log-log plot. The most anomalous behavior occurs when the scaling coefficient α reaches its smallest value, $\alpha_{\min}$. We find that $\alpha_{\min}$ decreases with filling fraction and binding energy (Figure 2.4c). Adding more obstacles and increasing the repulsion causes greater hindrance of tracer motion. We note that $\alpha_{\min} \approx 0.7$ near ν^l for impenetrable obstacles, as found previously [5, 30]. Finite repulsive binding energy leads to a smaller exponent ($\alpha_{\min} < 0.7$) than the infinite case at filling fraction above ν^l. For lower values of ΔG, the scaling coefficient does not go to zero at the upper critical occupancy ν^u. Note that the sharp cutoff with filling fraction occurs because we did not collect data past ν^u.

Sticky obstacles with attractive binding interactions show a more rapid falloff in the diffusion coefficient and larger anomalous time (Figure 2.4). The upper critical density $\nu^u \approx 0.72$ is in the same vicinity as for $\Delta G > 0$. The dependency of the diffusion coefficient on filling fraction for positive and negative binding energy are similar for low magnitude of the binding energy, but the diffusion coefficient falls off more rapidly with filling fraction for highly attractive obstacles. This occurs because an attractive obstacle confines a tracer in one position until it escapes, while a repulsive obstacle only impedes tracer motion for one time step. Therefore, repulsive interactions require several obstacles to transiently confine a tracer, while a single attractive obstacle can cause confinement. Note that we did not include large attractive binding free energy in our analysis.

For attractive obstacles, $\alpha_{\min}$ is independent of binding energy over the range we studied (Figure 2.4). The characteristic time for a tracer to unbind from an attractive obstacle depends on the binding energy, leading to the energy-dependent variation in the anomalous time we observe. However, it is properties of the obstacle arrangement, rather than of binding, which determine

the shape of the MSD curve, and therefore $\alpha_{\min}$. The minimum anomalous exponent occurs when tracers are, on average, confined to a cage formed by inter-obstacle boundaries and single-site wells. Therefore, the minimum anomalous exponent is approximately the same for all binding energy, but varies with filling fraction.

We note that the sticky soft obstacle model studied here does not simply map to impenetrable obstacles at a lower effective obstacle filling fraction. Such a mapping cannot be made because tracers can 'hop through' single obstacles via binding, while never being able to hop between obstacles. Sticky obstacles allow for move attempts—and blocks—that would never be attempted in the impenetrable case.

2.4.1   Sticky soft obstacles in 3D

We extended our study of single-site sticky repulsive obstacles to three dimensions, to determine whether the spatial dimension plays a key role in the tracer behavior (Figure 2.6). The results are qualitatively the same as the 2D model (Figure 2.4). However, in 3D, the lower and upper critical occupancies appear at higher filling fraction: a higher obstacle filling fraction is required to percolate a 3D lattice. The anomalous time is also typically smaller in 3D. For soft sticky obstacles, increasing the spatial dimension does not change the qualitative features of our model, but does shift the critical occupancies and anomalous time.

2.5   Slippery soft obstacles

When obstacles are perfectly slippery, bound tracers can hop to adjacent obstacles without penalty. Our model of perfectly slippery obstacles contains an occupancy-energy inversion symmetry: the dynamics are invariant to changing the filling fraction by switching obstacles and empty sites ($\nu \to 1 - \nu$) while simultaneously switching the sign of the binding energy ($\Delta G \to -\Delta G$). In other words, a low filling fraction of attractive obstacles is equivalent to a high filling fraction of repulsive barriers (Figure 2.7).

Slippery obstacles remove the obstacle percolation threshold for all measured binding energies

Figure 2.7: Slippery obstacles in 2D. (a, d) Diffusion coefficient D^*, (b, e) anomalous time t_a, and (c, f) minimum scaling exponent $\alpha_{\min}$ as a function of obstacle filling fraction ν for repulsive (top) and attractive (lower) binding energy. The approximate locations of the critical occupancies ν^l and ν^u are indicated with gray dotted lines.
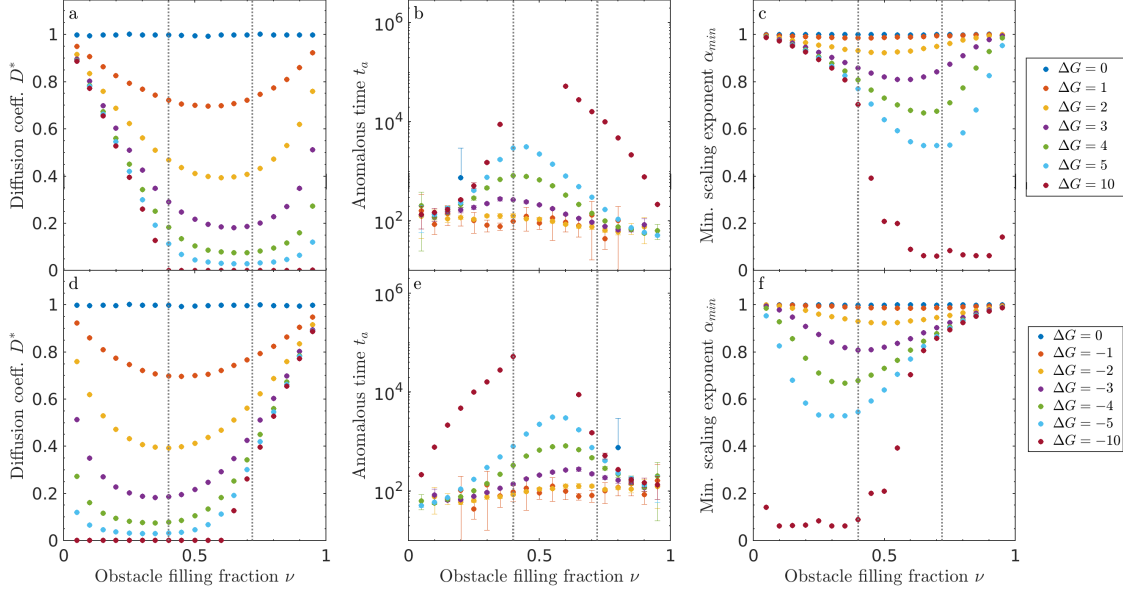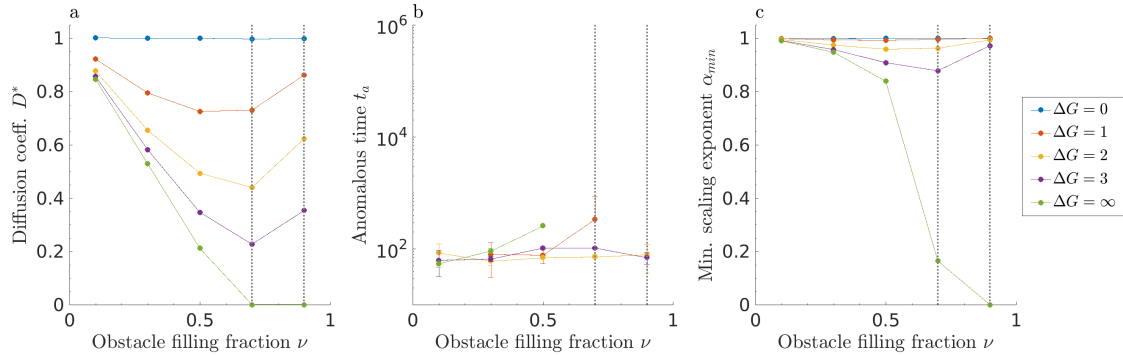

Figure 2.8: Slippery obstacles of size one in 3D. (a) Diffusion coefficient D^*, (b) anomalous time t_a, and (c) minimum scaling exponent $\alpha_{\min}$ as a function of obstacle filling fraction ν. The approximate locations of the critical occupancies ν^l and ν^u are indicated with gray dotted lines.

(Figure 2.7). The curves for $\Delta G = 10$ for the repulsive slippery obstacles qualitatively resemble the sticky case (Figure 2.4), because the diffusion coefficient approaches zero for $\nu \approx 0.4$. However, for slippery obstacles, the anomalous time increases, but does not diverge, at the percolation threshold, and then decreases at larger filling fraction. For slippery obstacles with finite ΔG, one can always find a time after which the system displays normal diffusion.

Figure 2.9: Comparison of models with slippery repulsive obstacles (solid lines), sticky repulsive obstacles (dashed lines), and hard repulsive obstacles (purple dashed line). (a) Diffusion coefficient D^*, (b) anomalous time t_a, and (c) minimum scaling exponent $\alpha_{\min}$ as a function of obstacle filling fraction ν. The gray dotted lines indicate the approximate locations of the critical occupancies ν^l and ν^u.
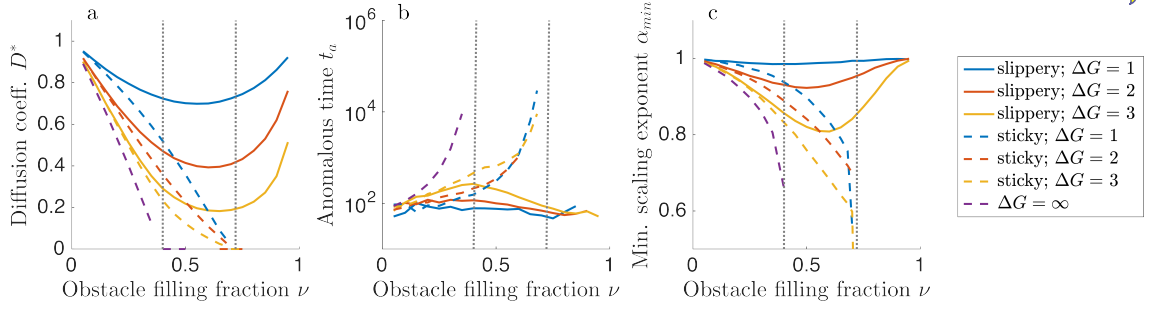
Slippery obstacles lead to non-monotonic behavior: for large enough ν, the diffusion coefficient increases and anomalous time decreases. For high obstacle filling fraction, binding increases tracer mobility, because tracers can hop along the percolating network of obstacles. Similarly, the minimum exponent is non-monotonic with filling fraction.

2.5.1   Slippery soft obstacles in 3D

As for sticky obstacles, we examined tracer motion with single-site slippery obstacles in three dimensions (Figure 2.8). The results are qualitatively the same as the 2D model (Figure 2.7), with typically smaller anomalous time. The occupancy-energy inversion symmetry noted above for two dimensions also holds in three dimensions. Therefore, the behavior for attractive obstacles can be extracted from Figure 2.8.

2.5.2 Comparison of sticky and slippery obstacles in 2D

The limits of perfectly sticky and slippery obstacles are most similar at low filling fraction (Figure 2.9). In general, slippery obstacles lead to exponents closer to one (less anomalous) than do sticky obstacles, because tracers are not caged by the obstacle-obstacle interface. Even for relatively small values of the binding energy ($|\Delta G| \leq 3$) and intermediate filling fraction, sticky and slippery obstacles lead to significantly different tracer dynamics (Figure 2.9). Slippery obstacles, on which motion can occur for high obstacle filling fraction, allow normal diffusion with coefficients comparable to those for low filling fraction. This effect may be important to explain the rates of a number of biological processes that are diffusion-limited, including transcriptional regulation and nucleo-cytoplasmic transport.

2.6 Semi-slippery obstacles

Having compared the limits of perfectly sticky ($D_{\text{bound}} = 0$) and slippery ($D_{\text{bound}} = D_{\text{free}}$) obstacles, we now study intermediate cases. We varied the bound diffusion coefficient for repulsive binding energy $\Delta G = 1, 2, 3, \infty$ and filling fraction $\nu = 0.3$ and 0.6. We chose these values to illustrate how our results change from the sticky to the slippery case, as shown in Figure 2.9. For finite binding energy, increasing D_{bound} increases the long-time diffusion coefficient (Figure 2.10). This effect is larger for higher filling fraction and lower binding energy, when tracers spend more time bound. Varying D_{bound} has little effect on the anomalous time at low filling fraction, because t_a is already near the threshold at which we can accurately measure it. However, increasing D_{bound} decreases t_a at higher filling fraction, because tracers can more quickly escape obstacles when their bound diffusion coefficient is larger. Similarly, varying D_{bound} has little effect on $\alpha_{\min}$ at low ν, but does make diffusion less anomalous at higher filling fraction, because increasing bound motility reduces tracer caging.

Figure 2.10: Semi-slippery obstacles in 2D. We varied the bound diffusion coefficient from the sticky limit $D_{\text{bound}} = 0$ to the slippery limit $D_{\text{bound}} = D_{\text{free}}$ for single site obstacles. (a, d) Diffusion coefficient D^*, (b, e) anomalous time t_a, and (c, f) minimum scaling exponent α_{min} as function of D_{bound} for low filling fraction $\nu = 0.3$ (top) and high filling fraction $\nu = 0.6$ (bottom).
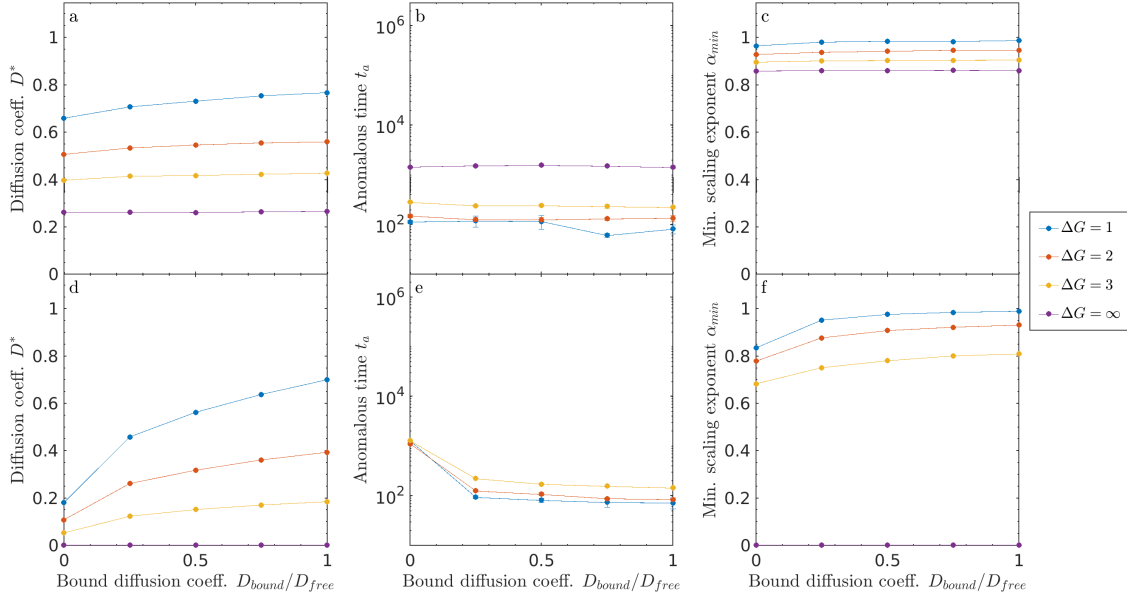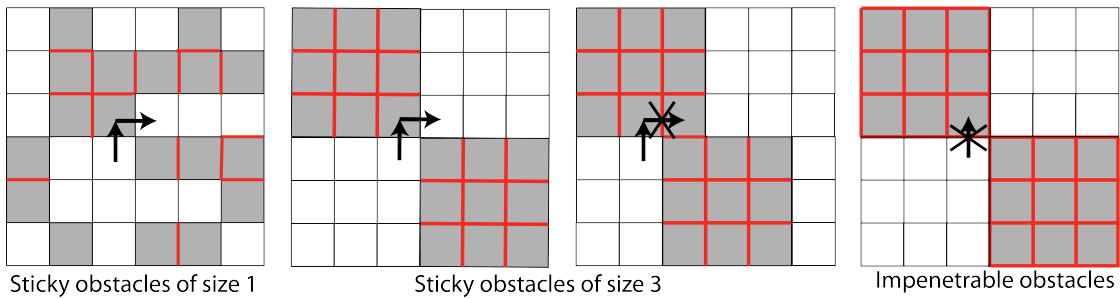

Figure 2.11: Cartoon showing size effects for sticky and impenetrable obstacles. Red lines indicate borders between obstacles that cannot be crossed by a tracer.

2.7 Varying obstacle size

We varied the length of the obstacles l_{obst}, while maintaining their square shape. Increasing the obstacle size (with filling fraction fixed) clusters obstacles. Since in our model the binding penalty occurs only for **empty** $\rightarrow$ **obstacle** moves, increasing the size of obstacles effectively reduces the number of binding sites: more obstacle sites are interior to obstacles, rather than on their perimeter. For sticky obstacles with $l_{obst} = 1$, tracers can easily hop through cages, since their bound motion is only blocked by an obstacle-obstacle interface. Increasing the obstacle size guarantees that individual obstacles will contain an obstacle-obstacle interface, which makes it less likely that tracers can hop through neighboring obstacles (Figure 2.11). Increasing obstacle size at fixed filling fraction also increases the typical distance between obstacles. These changes alter obstacle percolation effects: ν^l and ν^u depend on l_{obst}.

2.7.1 Sticky obstacles of varying size

First, we examined tracer dynamics on sticky obstacles of variable size (Figure 2.12). Qualitatively, large sticky obstacles have a soft surface (binding can occur on surface sites, although hops along the surface are still blocked), but a hard core (interior sites are inaccessible). A significant change in dynamics occurs when l_{obst} increases above 1. Any obstacle with $l_{\text{obst}} > 1$ is fundamentally different from $l_{\text{obst}} = 1$, because larger obstacles are guaranteed to contain sites with an adjacent obstacle site. Increasing l_{obst} prevents hopping across the interior of any one obstacle, which can hinder tracer motion. The cages are thus more robust. Tracers can still hop across corners, unlike in the case of a purely repulsive interaction (Figure 2.11).

The dependence of tracer dynamics on binding energy changes upon increasing the obstacle size above 1 (Figure 2.12). For size-one obstacles, particles can hop through a single obstacle, and so lower binding energy leads to higher long-time diffusion coefficient. In contrast, with larger obstacles, high binding energy leads to an increased diffusion coefficient. With higher repulsion, a tracer is less likely to bind to the surface of an obstacle where it can get stuck. Thus, for larger

obstacles, higher repulsion can facilitate motion.

For $l_{\text{obst}} > 3$, increasing obstacle size increases the cage size, and so the long-term diffusion coefficient and the anomalous time both increase smoothly, in agreement with previous work on impenetrable obstacles [36]. The anomalous time increases with l_{obst} above 3, because the effective cage size increases: tracers take longer to explore a cage to escape. For $l_{\text{obst}} \geq 3$ and small filling fraction, the size dependence is roughly energy independent. The dynamics are dominated by blocked **obstacle $\rightarrow$ obstacle** moves, rather than by the energy dependence of **empty $\rightarrow$ obstacle** moves. For low filling fraction, α_{min} remains > 0.9, suggesting that obstacle caging effects are minimal.

Figure 2.12: Size effects for sticky obstacles in 2D. (a, d) Diffusion coefficient D^*, (b, e) anomalous time t_a, and (c, f) minimum scaling exponent α_{min} as a function of obstacle filling fraction ν for $\nu = 0.3$ (top) and $\nu = 0.6$ (lower).
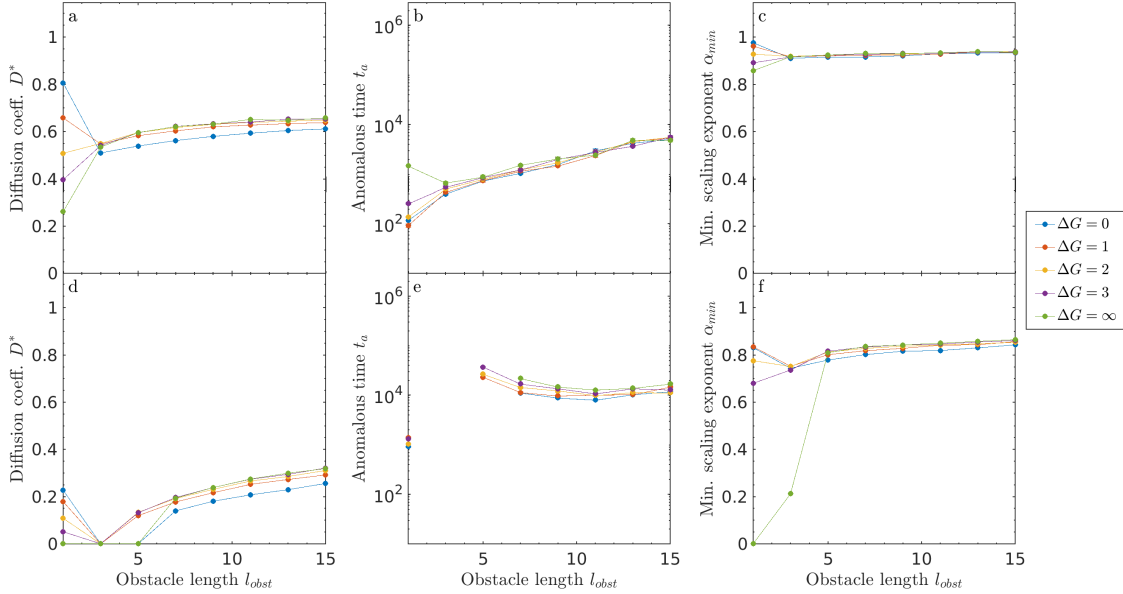
Next, we examined a higher packing fraction $\nu = 0.6$, chosen because it is between ν^l and ν^u for size-1 obstacles in 2D. The effects of obstacle size on percolation are significant, leading to larger changes in behavior than for $\nu = 0.3$. As l_{obst} increases, obstacles are on average spaced farther apart, which increases ν^l.

In contrast, the upper critical concentration is more complicated, because now each obstacle contains within it obstacle-obstacle interfaces. The upper critical concentration decreases below 0.6 for $l_{\text{obst}} = 3$, and therefore the dynamics are anomalous at all times; t_a diverges and D^* goes to zero. Above $l_{\text{obst}} = 3$, the upper critical concentration increases with increasing obstacle size. For $l_{\text{obst}} = 5$, $\nu^u > 0.6$, leading to long-time Fickian diffusion. Here t_a decreases with l_{obst}, because the time required for a tracer to escape a cage is not dominated by the cage size (as it was for low ν), but by the time needed to find a gap between cages. As l_{obst} increases, the gaps become larger on average, lowering the escape time. Overall, above $l_{\text{obst}} = 5$, the behavior is only mildly dependent on either obstacle size or binding energy, making the long-time diffusivity primarily a function of the filling fraction.
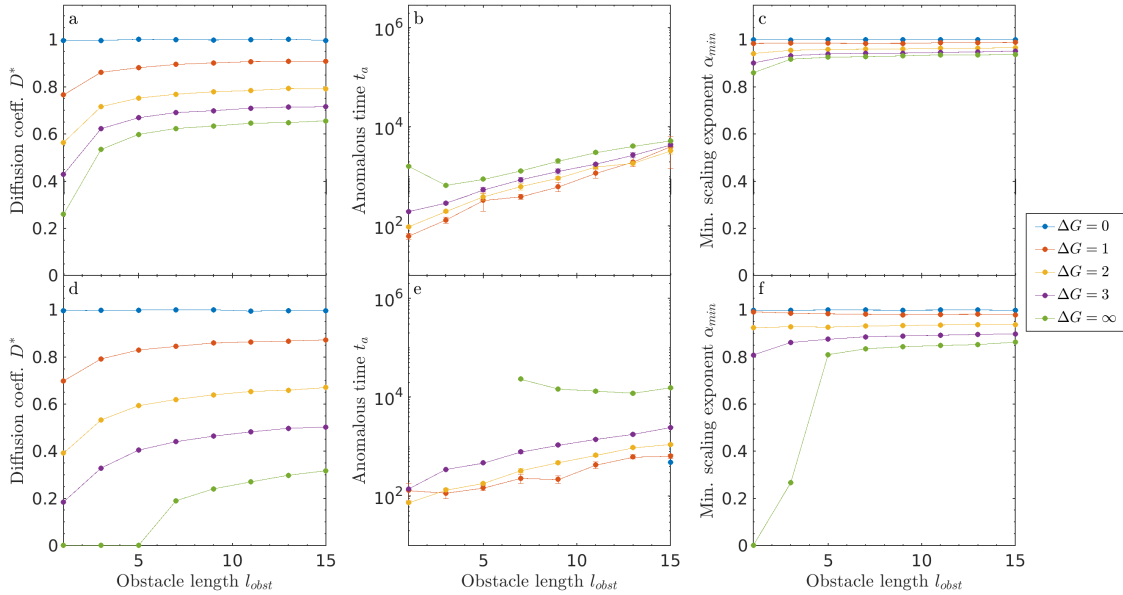
Figure 2.13: Size effects for slippery obstacles in 2D. (a, d) Diffusion coefficient D^*, (b, e) anomalous time t_a, and (c, f) minimum scaling exponent $\alpha_{\min}$ as a function of obstacle filling fraction ν for $\nu = 0.3$ (top) and $\nu = 0.6$ (lower).

2.7.2   Slippery obstacles of varying size

Understanding the effects of variable obstacle size on tracer motion is more straightforward for the case of slippery obstacles, because the difference between edge and interior obstacle sites is eliminated (Figure 2.13). In the perfectly slippery limit, increasing l_{obst} effectively lowers the number of binding sites: tracers experience the binding energy change only when binding to obstacle edge sites, but can move freely through obstacle interior sites. Therefore, D^* and α_{min} increase with obstacle size, an effect that is larger for higher filling fraction, because obstacle overlaps at high filling fraction lower the fraction of obstacles that impede motion and cage tracers. In nearly all cases, t_a increases with obstacle size, because the effective cage size grows. The exception occurs for impenetrable obstacles, where increasing l_{obst} increases the size of vacancies between cages, allowing caged tracers to escape more quickly.

2.8   Conclusion

In this paper, we have studied a lattice model of tracer particles that diffuse and experience crowding due to immobile obstacles. While most previous work has considered hard (impenetrable) obstacles, we consider soft (penetrable) obstacles characterized by a binding free energy that allows tracers to overlap with obstacles. We also consider the effects of varying the tracer mobility while bound, including the limiting cases of 'sticky' obstacles (which immobilize bound tracers) and 'slippery' obstacles (which allow full tracer mobility), as well as the intermediate regime between the two.

In some cases, diffusion in crowded media leads to dynamics that are anomalous ($r^2 \sim t^\alpha$) with a constant α [2]. However, our system typically does not give a power-law dependence of the MSD on time delay; this has been seen by others [9, 38]. As a result, we quantified a long-time diffusion constant (D^*), the timescale on which the systems transitions from anomalous to Fickian (t_a), and the minimum instantaneous anomalous exponent (α_{min}).

Our results demonstrate the key differences between sticky and slippery obstacles. For sticky

obstacles, increasing the obstacle filling fraction decreases the diffusion coefficient and increases the degree of anomalous diffusion. Above an upper critical occupancy $\nu^u \approx 0.72$ in 2D, diffusion becomes anomalous at all times, independent of binding energy. In the sticky case, the minimum anomalous exponent $\alpha_{\min}$ monotonically decreases with filling fraction, because adding obstacles creates more cages in which tracers become transiently confined.

For slippery obstacles, by contrast, tracers always reach normal diffusion after a sufficiently long time; even increasing the filling fraction above the percolation threshold does not eliminate tracer motion. For nonzero binding free energy, we find a novel non-monotonic dependence of D^* on filling fraction: increasing the filling fraction away from zero introduces binding sites that slow tracer diffusion, but for sufficiently high filling fraction, bound mobility allows tracer motion along clusters of obstacles. The anomalous exponent decreases with binding energy magnitude, but varies non-monotonically with filling fraction. For low filling fraction, $\alpha_{\min}$ decreases as more obstacles are added, because binding transiently traps tracers on isolated obstacles. For sufficiently high density, diffusion becomes more normal when tracers hop along clusters of obstacles while bound.

For intermediate 'semi-slippery' obstacles, we demonstrate that in the crossover from sticky to slippery behavior, D^*, $\alpha_{\min}$, and t_a vary smoothly. Increasing bound diffusion always makes the diffusion coefficient larger and the diffusive motion less anomalous.

We varied obstacle size to examine how relatively large obstacle domains affect tracer motion in our model. For sticky obstacles, increasing obstacle size above 1 led to a sharp jump in tracer properties. This occurs because larger obstacles always contain interior obstacle sites, which are inaccessible to tracers in the sticky model. For large obstacles, increasing repulsive binding energy tends to increase the tracer diffusion coefficient, because tracers spend less time trapped in a binding site.

For slippery obstacles, perimeter and interior obstacle sites are both accessible, which means that varying obstacle size has effects that are easier to understand intuitively. The diffusion coefficient and anomalous exponent increase with obstacle size, because larger obstacles lead to a fewer obstacle-empty boundaries. The effect of obstacle size on t_a varied with filling fraction, due to

competing effects on increasing cage size and increasing gaps between cages.

Our models separately represent effects of soft interactions (through the binding energy) and bound-state motion (through obstacle stickiness/slipperiness). Sticky and slippery obstacles show dramatically different tracer dynamics, even at short time and low filling fraction. Slippery obstacles lead to a diffusion coefficient which varies non-monotonically with filling fraction, with high values at both high and low obstacle density. As the filling fraction increases from zero, tracers are more and more inhibited by obstacles. However, as the obstacle density increases, particles which bind can more easily move between obstacles. This may describe transport factor motion within the nuclear pore complex, where transport factors can slide on the disordered FG Nups [47]. Therefore, biological systems may use soft interactions and slippery obstacles to allow particle diffusion, even in the highly crowded cellular interior.

Our work highlights how soft interactions and bound-state mobility can dramatically change tracer motion. These effects are relevant to biological systems, ranging from membraneless organelles to lipid rafts. Although most previous theoretical work on crowded diffusion has focused on the anomalous exponent, these biological examples highlight the importance of changes in the diffusion coefficient. For example, proteins which do not passage through the nuclear pore complex on biologically relevant time scales (minutes to hours) cannot have biological effects, and so the speed of passage is the fundamentally important biological quantity. The long-time diffusion coefficient varies dramatically in our model between hard obstacles, soft sticky obstacles and soft slippery obstacles (Figure 2.9). Thus, the effective permeability of obstacles and the degree to which bound particles can diffuse can be used by cells to tune macromolecular motion.

Chapter 3

Biofilter modeling

Filters composed of biopolymers ~~are found to~~ selectively control the transport of molecules, nanoparticles, viruses, and other organisms in both living and synthetic systems [1]. Examples of these filters include the nuclear pore complex or NPC, the pericellular matrix is cells, the extracellular matrix in tissues, and mucus in organs. These filters will allow passage or certain particles while blocking others. By acting as a physical barrier, it can protect certain system but also inhibit drug delivery—*e.g.*, microbial biofilms sequestering antibiotics [79] and mucosal limiting drug delivery in cancer and other diseases [1]. The role of binding and bound motion remains unclear. Binding in certain cases can inhibit motion. Mucus inhibits the transport of nanoparticles in airways [80–82]. Certain viruses can minimize binding under certain circumstances which can allow human papillomavirus and human immunodifficiency virus to pass through cervical mucus [83, 84]. Antibodies fight this effect by binding to viruses and slowing ~~down~~ these interactions [85], indicating that binding inhibits motion. In other cases, binding can facilitate transport. In the nuclear pore complex, transport factors that bind to proteins can move through rapidly [86]. Similarly, binding can enhance the cellular uptake of nanoparticles through entrapment and accumulation [87]. In order to improve the design of synthetic filters, the role of binding and bound motion needs further investigation. Work has done to study the effects of particle size, charge, and binding interactions [1]. However, the physical principals that affect transport across these filters is not well understood.

Among these filters, the NPC is tuned for selective passage enabled by binding. The NPC selectively filters molecular traffic between the nucleus and cytoplasm of eukaryotic cells, making

it important for diverse processes including gene regulation and translation [86]. Transport occurs through the central channel, ∼50 nm in diameter and ∼100 nm long. The selective barrier filling the central channel is made from disordered proteins, the FG nucleoporins (FG Nups), which contain repeated phenylalanine-glycine (FG) motifs Figure 3.1. Transport factors (TFs) that directly bind to the FG repeats can cross the NPC and carry cargo with them [86]. Transport through the NPC is remarkably fast, with pore residence times ∼10 ms [88]. Binding between FG Nups and TFs shows diffusion-limited on-rates and transient binding of individual FG repeats to TFs [46, 89]. How the FG Nups both block passage (of non-binding molecules) and facilitate passage (of binding molecules) is not fully understood, making the NPC an ideal system to dissect the principles of binding-controlled selective transport.

The work in the previous chapter stressed the importance of inhomogeneities into ~~the systems causing complex dynamics like~~ anomalous diffusion. In this chapter, we ~~will take a different approach to studying~~ transport across biofilters by analyzing the bulk-continuum behavior of particle concentration. We ~~will~~ assume that ~~our~~ obstacles form a homogeneous continuum in which tracers can bind ~~to~~ at any given location. Once bound, a tracer may also exhibit bound motion. ~~The dynamics mentioned are described by a reaction diffusion equation. Here, will discuss how reaction diffusion equations can be used as a framework to study transport across biofilters. After presenting the model, we will demonstrate how it was used to study transport across the nuclear pore complex.~~

3.1   Reaction diffusion and selectivity in biofilters

In this section, we ~~will lay out~~ a minimal model that can be used to ~~measure~~ transport across biofilters. We ~~will~~ present a ~~general~~ framework for a tracer's ~~equations of~~ motion in a biofilter and apply this tool to study selectivity in the NPC. ~~Our minimal model is in terms of physical parameters that correspond to microscopic interactions.~~

Our model applies to is described in Figure 3.1. Particles ~~are diffusing in~~ with ~~some~~ coefficient D_F in a one dimensional box~~, sometimes referred to as~~ gel, of length L. The box is filled with ~~a homogeneous landscape of~~ binding sites at concentration N_T with a binding on-rate ~~of~~ k_{on} and off-

Figure 3.1: Schematics of the nuclear-pore complex and model. (A) The nuclear pore complex (gray) is filled with FG Nups (green polymers) that selectively passage transport factors that bind to FG Nups (blue) while blocking non-binding proteins (red). The central channel of the pore has length L. Protein concentration is high on the left (inlet) and low on the right (outlet). (B) Selectivity quantifies the degree of selective transport through the pore. A non-selective pore with $S = 1$ has the same flux for a transport factor as for a non-binding protein (top). A selective pore with $S > 1$ has a larger flux for a transport factor than a non-binding protein (lower). (C) The bound diffusion coefficient quantifies the mobility of a bound transport factor. A transport factor may be immobile (top) or mobile (lower) when bound. Figure created by Laura Maguire and used with permission.
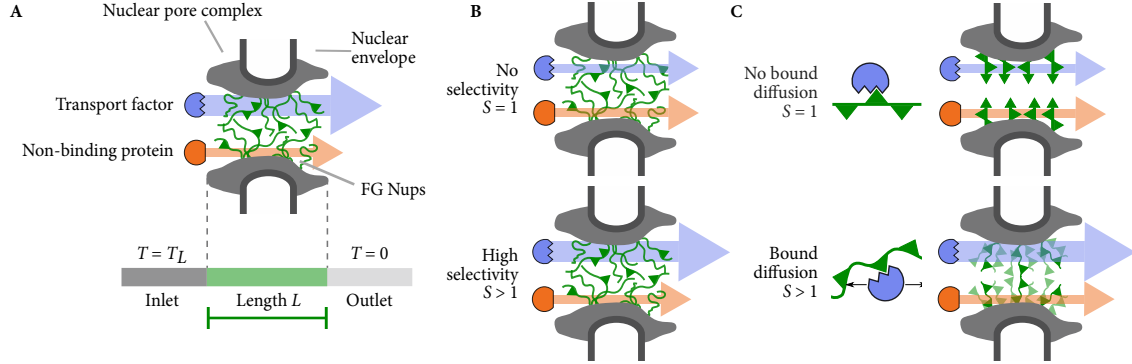
rate k_{off}. ~~These are related to~~ the dissociation constant ~~by~~ $K_D = \frac{k_{\text{off}}}{k_{\text{on}}}$. The free species ~~is described by some~~ concentration~~s~~ T while the bound species ~~is described by some bound complex~~ C. In the NPC ~~case~~, these binding sites correspond to polymers (FG nucleoporins or FG nups) ~~in~~ which proteins called transport factors T can bind to while other proteins cannot. The concentration of the inlet and outlet ~~is~~ fixed ~~Dirchlet boundary conditions~~ to T_L and 0, respectively. Once bound, the complex can diffuse (D_B). Since the binding sites are immobile, the bound species has no flux ~~Von Neumann~~ boundary conditions. ~~Binding sites can fill up. Therefore,~~ the number of free binding sites ~~at a given location~~ is $N(x) = N_T - C(x)$. ~~We are interested in how binding and bound diffusion alters the selectivity of the pore. A continuum equation for~~ this system is ~~given~~ by ~~a~~ reaction diffusion equation

$$\frac{\partial T}{\partial t} = -k_{\text{on}}TN + k_{\text{off}}C + D_F\frac{\partial^2 T}{\partial x^2}, \tag{3.1}$$

$$\frac{\partial C}{\partial t} = k_{\text{on}}TN - k_{\text{off}}C + D_B\frac{\partial^2 C}{\partial x^2}. \tag{3.2}$$

The ~~first~~ two terms in Eqn. 3.1 and 3.2 correspond to the reaction kinetics while the last term describes diffusion. ~~A clarification on the bound diffusion should be mentioned.~~ The actual binding sites do not diffuse ~~they are static~~. The complex—a particle bound to a site—diffuses. Meaning, a bound particle can transfer across binding sites without ever unbinding.

A natural question may arise: how does this system correspond to the previous lattice model (Chapter 2)? In the previous model, inhomogeneities in the system introduced memory effects that caused anomalous diffusion. Obstacles excluded some volume at a specific location. Here, particles can bind anywhere, and obstacles cannot block a step attempt. Rather, there is a chance that a tracer will bind at a given timestep without changing its position. We can image this as a dual-lattice system: one lattice corresponds to a free state and another corresponds to a bound state. When free, a particle undergoes a random walk on the free-state lattice. There is a probability to bind to the other lattice. When it does, it stays at the same position but on the bound-state lattice. Similarly, it can hop back to the free-state to from the bound-state lattice. These binding probabilities correspond to k_{on} and k_{off}, and differing step rates on the lattices are related to the

diffusion coefficients.

~~We are interested in how selective a filter is.~~ The particle flow into the outlet is given by the flux, $J = \frac{\partial T}{\partial x}\big|_{x=L}$. ~~The outlet flux was normalized by the steady-state flux for the non-binding case.~~ As particles diffuse across the gel, the ~~normalized~~ flux will ~~change in time until the system~~ reaches a steady state. We define the selectivity as

$$S = \frac{J_{\text{binding}}(t \to \infty)}{J_{\text{non-binding}}(t \to \infty)}. \tag{3.3}$$

The selectivity describes how many more ~~(as multiple factor)~~ particles ~~are~~ flowing into the outlet in steady state relative to ~~the~~ non-binding ~~case~~. A filter is selective if it has some ability to let certain particles through while block others. ~~By tuning the kinetic and diffusive parameters, the selectivity of a biofilter is altered.~~

3.1.1 Numerics and properties

Figure 3.2: Flux through the pore and selectivity for TFs with varying bound mobility. (A) Flux as a function of time when TFs are immobile while bound, with varying binding affinity as in (B). (B) Flux as a function of time when TFs are mobile while bound with $D_B = D_F$, with varying binding affinity. (C) Selectivity as a function of dissociation constant with varying bound diffusion coefficient.
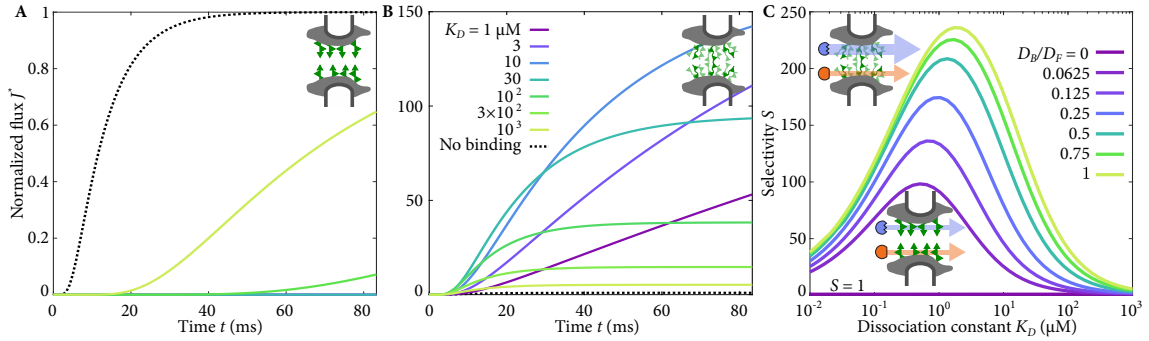
~~Before delving into the numerical solutions, certain behavior can be extracted analytically from Eqn. 3.1 and 3.2.~~ First, we can ~~look at~~ the solution ~~to~~ absence of binding. The steady state solution ~~for the diffusion equation with Dirichlet boundary conditions~~ is ~~simply~~

$$T(x) = \frac{T_L(L-x)}{L}; \qquad J = \frac{D_F T_L}{L}. \tag{3.4}$$

Figure 3.3: (A, B) Selectivity as a function of diffusion coefficient ratio, with varying dissociation constant, in the full nonlinear model (A) or in the linear approximation (B). (C) Selectivity as a function of dissociation constant, with varying diffusion coefficient ratio, in the linear approximation. The region to the left of the dotted line is non-physical; the full nonlinear solution should be used.
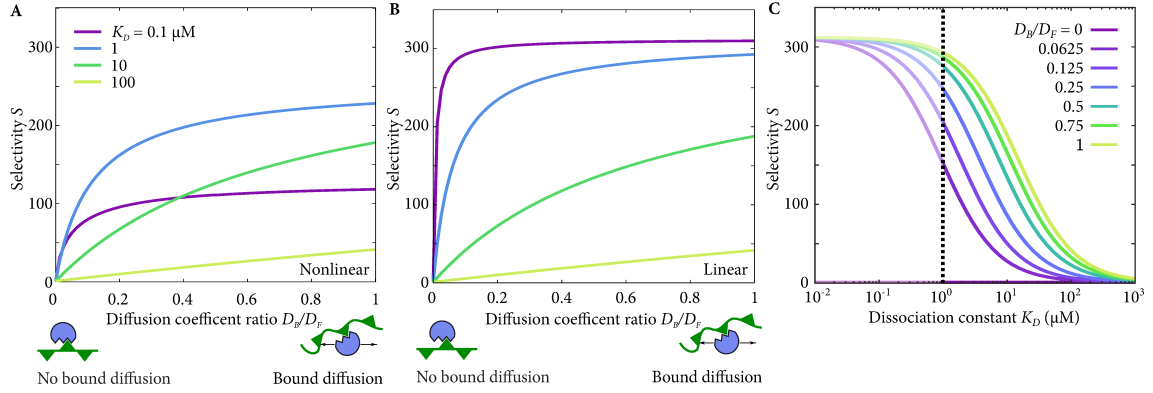
Also when $D_B = 0$, the unbound species steady state concentration must be also be linear (Eqn. 3.4). ~~We can already make some profound predictions about the role of bound motion within this model: in its absence~~, the reaction kinetics do not play a role in selectivity. While kinetics cannot alter the steady state density profile, it can influence dynamics.

We ~~can~~ investigate ~~the role of~~ the non-linear coupling term $T(x)C(x)$ (Eqn. 3.1, 3.2) by comparing the linear and full solutions (Figures 3.2, 3.3). When $C(x)/N_T$ is small compared to one, the model is linear. When it's large, non-linearities play a role. Physically, this corresponds to binding site saturation. A linear model assumes that binding sites can always accept another binding complex. This can lead to unphysical results if the concentration of the bound complex exceeds the concentration of binding sites. ~~We can tease out the linear condition by considering the bound complex being in chemical equilibrium with T — i.e., we ignore diffusive terms.~~ In chemical equilibrium,

$$Ck_{\text{off}} = k_{\text{on}}A(N_T - C). \tag{3.5}$$

~~We can rearrange this equation to find~~ the linear condition

$$\frac{C(x)}{N_T} = \frac{1}{K_D/T(x) + 1} \ll 1. \tag{3.6}$$

The maximum ~~value~~ of the free species occurs at the boundary $T = T_L$. Therefore, our system is linear when

$$\frac{T_L}{K_D} \ll 1. \tag{3.7}$$

When this condition is met, we can drop the non-linear term in the coupled reaction diffusion equations. ~~In doing so,~~ we can solve for the linear solution of the free species ~~as~~

$$T(x) = b + mx + fe^{\lambda x} + ge^{-\lambda x}, \tag{3.8}$$

where $\lambda^2 = k_{\text{off}}(D_F + N_t K_A D_B)/(D_F D_B)$ and b, m, f, g are coefficients fixed from boundary conditions (Appx. C.1). In the NPC, experimentally measured flux is typically linearly proportional to TF concentration [90,91], TF concentration likely remains below binding saturation in the NPC ~~and are in the linear limit.~~

As for the numerics, the coupled reaction diffusion equations can be written is a vectorized form as

$$\frac{\partial a}{\partial t} = L_{op}a + W_{op}(a),$$ (3.9)

where $a = [T(x)\, C(x)]'$, L_{op} is the linear component of the differential operator and $W_{op}(a)$ is a non-linear function of a. We interested in evolving the temporal dynamics as well as the steady state solution in order to determine the selectivity of a biofilter. We numerically integrate this time-dependent reaction-diffusion equations using Crank-Nicolson stepping for the linear portion and forward Euler for the non-linear portion:

$$a_{n+1} = a_n + \delta t L_{op}(a_n + a_{n+1})/2 + W_{op}(a_n)\delta t.$$ (3.10)

The numerical integration was implemented in MATLAB. We numerically found steady state solutions of the equations

$$\frac{\partial}{\partial x}\begin{bmatrix} T \\ C \\ T_x \\ C_x \end{bmatrix} = \begin{bmatrix} T_x \\ C_x \\ \frac{1}{D_F}\left[k_{\mathrm{on}}T(N_T - C) - k_{\mathrm{off}}C\right] \\ -\frac{1}{D_B}\left[k_{\mathrm{on}}T(N_T - C) - k_{\mathrm{off}}C\right] \end{bmatrix},$$ (3.11)

where the x subscript refers to partial differentiation with respect to x, using the differential equation solver bvp5c in MATLAB. There is an enormous numerical advantage to solving the ODE over the full PDE, but you lose all of the temporal information. Whenever we were interested in the dynamics, we solved the full PDE; all of the selectivity measurements were found by numerically integrating the ODE (Eqn. 3.11).

3.2 Transport measurements in the nuclear pore

With the theory in place, we can apply our biofilter model to the NPC. We consider a minimal model of the central channel of the NPC containing FG Nups homogeneously anchored (Figure 3.1). This model is sufficiently general to describe the common features of a range of biopolymer filters. The NPC, unlike most other biopolymer filters, has a wide capture area that may increase transport

Table 3.1: Comparison between experimental results for NTF2 and GFP (a similarly-sized non-binding protein) and model predictions. Flux measured in units of molecules per pore per second.

Method	Cell type	Species	Flux	Selectivity	Notes
OSTR	*Xenopus*	NTF2	91–123	24–37	[92]
		GFP	3.3–3.8		
OSTR	*Xenopus*	NTF2	47.3	43	[93]
		GFP	1.1		
Permeabilized cells	HeLa	NTF2	250	125	[94]
		GFP	2		
Model	–	Binding	2–480	1–240	This work
		Non-binding	2		

Figure 3.4: Dependence of flux on variation of individual parameters: (A) on-rate constant, (B) total FT Nup concentration N_t, (C) inverse of the free diffusion coefficient, and (D) pore length, with varying dissociation constant. All values calculated in the linear approximation. Bound diffusion coefficient $D_B = 0.1 D_F$. Other parameters fixed at the values of section Appx. C.2.
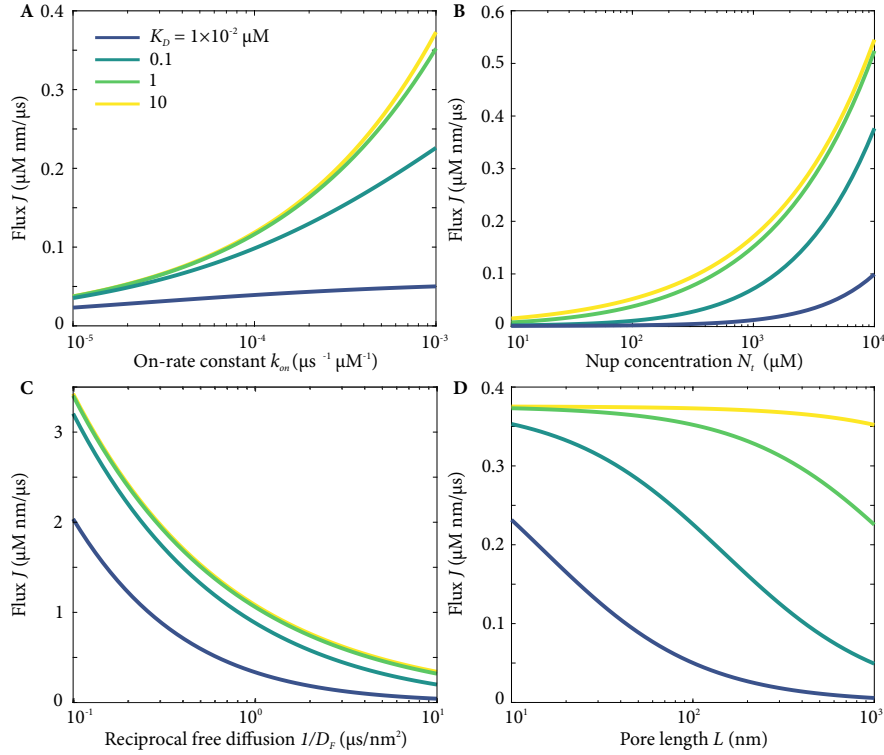
rates [95]. In order to focus on basic principles of transport, we neglect this effect. A varying free energy landscape along the axis of the NPC may play a role in selective transport [48, 96–98].

Figure 3.5: Dependence of selectivity on variation of individual parameters: (A) on-rate constant, (B) total FT Nup concentration N_t, (C) inverse of the free diffusion coefficient, and (D) pore length, with varying dissociation constant. All values calculated in the linear approximation. Bound diffusion coefficient $D_B = 0.1 D_F$. Other parameters fixed at the values of section Appx. C.2.
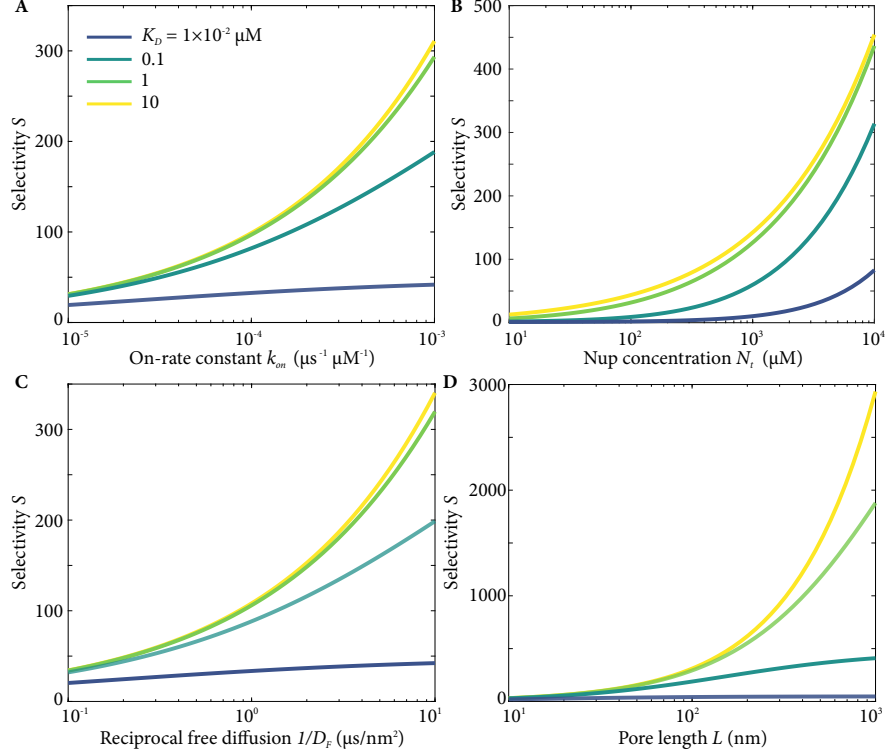
However, the NPC is robust to deletion of all asymmetric Nups and many Nup combinations, indicating that spatial variation in pore properties is not necessary [99, 100]. Experiments *in vitro* with simplified, homogeneous Nup composition produced selective transport [101, 102].

Rapid transport requires TF-FG Nup binding, while a protein similar to a TF but unable to bind FGs is excluded. Therefore, in our model we compare two proteins that are identical, except that one binds FG Nups and the other does not. As a model TF, we consider nuclear transport factor 2 (NTF2) [103]. NTF2 is small ($\sim$5 nm) relative to the diameter ($\sim$50 nm) and length of the pore ($\sim$100 nm), suggesting that passage of NTF2 does not require large-scale molecular rearrangements that have been proposed for larger molecules [104, 105]. Because of the small size of NTF2 we neglect effects of steric crowding, which can enhance selectivity in a transport model [96]. NTF2 appears

not to be actively released from the pore, suggesting that selective transport is an intrinsic property of the NPC [96, 106], and in contrast to actively released karyopherins [104, 106–108].

Transport through the NPC requires entry into the pore, passage, and exit. In single-molecule measurements, most of the transport time is spent in a random walk within the central channel [88, 98]. We therefore assume that entry and exit rates are determined by binding kinetics. The directional bias in TF transport is controlled outside the NPC through a concentration difference between the nucleus and cytoplasm generated by the Ran-GTP system [109]. In our model, we impose a fixed concentration difference across the pore.

We consider a channel of length L filled ~~homogeneously~~ with Nups that separates two reservoirs (Figure 3.1A). Within the channel are free transport factor (concentration T), free FG Nups (N), and bound TF-FG complex (C), with total Nup concentration $N_t = N + C$. TF diffusion within the channel ($0 < x < L$) is described by the reaction-diffusion equations (Eqn. 3.1, Eqn. 3.2). TF-FG interaction has on-rate constant k_{on}, off-rate k_{off}, and dissociation constant $K_D = k_{\text{off}}/k_{\text{on}}$. We include competition between TFs for FG binding sites [48]. The diffusion constants of free (D_F) and bound (D_F) TFs are spatially constant. The fixed reservoir TF concentrations are T_L (inlet, left) and 0 (outlet, right).

3.2.1 No selective transport occurs if bound TFs are immobile

If TF-FG Nup binding immobilizes the TF, the bound-state diffusion coefficient $D_B = 0$. For immobile bound TFs, transport is not selective: the steady-state flux $J = D_F T_L / L$ for both binding and non-binding proteins, so $S = 1$ (Figure 3.2, 3.3). The binding TF accumulates within the pore, but its immobility means it does not enhance transport compared to the non-binding case. Notably, this effect is independent of binding kinetics. Prior to steady state, binding slows transport (Figure 3.2A). In systems such as airway mucus, immobilization may increase the time available for degradation or active clearance, consistent with the observation that binding tends to inhibit selective transport in those systems [80–82]. This effect is related to the binding-site barrier seen in antibody delivery to tumors [110], and observations that non-binding nanoparticles

are often more effective in drug delivery to tumors than binding particles [1].

3.2.2   Bound-state diffusion allows selective transport

When bound TFs are mobile, selective transport occurs with a selectivity up to 240 for a conservative set of parameters (Figure 3.2B,C, 3.3, C.2). Remarkably, this selectivity is comparable to experimental measurements of NTF2 versus GFP flux (Table 3.1). The interplay between binding kinetics and diffusion leads to an optimal dissociation constant ~ 1 μM for maximum selectivity (Figure 3.2C). Selectivity decreases for high K_D because binding is too weak to significantly increase TF concentration in the pore. For low K_D, tight binding causes the concentration of bound complexes to become approximately constant across the pore. Because diffusive flux is driven by a concentration gradient, this washing out of the gradient by tight binding decreases flux and selectivity.

Our model predicts that selectivity is increased by increasing binding on-rate constant k_{on} Figure 3.5. Consistent with this, the on-rate constants of TF-FG Nup interactions have been measured to be diffusion limited [46, 89]. Large k_{on} makes transport more selective because fast binding kinetics relative to diffusive motion are necessary to maintain steep concentration gradients within the pore. High FG Nup concentration (as measured experimentally) leads to large N_t and low D_F, both of which increase selectivity. Decreasing D_F or increasing the length of the pore both reduce the magnitude of the flux and increase selectivity (Figures 3.5, 3.4). Therefore, varying TF free diffusion coefficient and pore length involves a trade-off between transit time and selectivity.

~~Here, we presented a model for biofilters and showed selectivity results for the NPC. In the following chapter, we will delve more into the nuclear pore complex. We will present two models for bound motion and how they influence selectivity.~~

Chapter 4

Selectivity and bound transport mechanisms in the nuclear pore complex

Models of the NPC selective barrier have proposed that the FG Nups may form an entropic brush [111], a dynamic hydrogel [94, 112], an intermediate state between a brush and gel [113], or liquid droplets [91]. These mechanisms may be modulated by spatial organization [114, 115] and binding of TFs to multiple FG repeats [104, 116]. Attempts to distinguish these models have been hindered by the pore's small size, the redundancy and multiple copies of FG Nups, and contradictory experimental results on FG Nups and TF binding [113]. Some FG Nup fragments form less-dynamic hydrogels *in vitro* [112], but remain highly dynamic within cells [46]. Molecular dynamics simulations find highly dynamic FG Nups, though the degree and extent of motion depends on the affinity of FG repeats for each other and for TFs [113, 117]. Crowding and competition modulate affinity [118] and may contribute to selective transport [96]. However, the connection between the amino-acid level behavior of the FG-TF interaction and macroscopic transport selectivity remains unclear. Here we address the central contradiction of selective transport through the NPC: how does binding of TFs to FG Nups within the pore increase the flux rather than decreasing it [1, 119]?

Using a biophysical model, we demonstrate that TF diffusion and binding are sufficient for selective transport, as long as binding only partially immobilizes TFs. Binding increases the local concentration, and these molecules contribute to the flux if mobile. Thermally-driven diffusion of TFs bound to flexible tethers gives sufficient particle mobility to produce selectivity similar to experimental measurements. Tether flexibility also allows bound TFs to hop between tethers, further enhancing selectivity.

4.1   Mechanisms of bound transport factor mobility

Table 4.1: Predicted selectivity of FG Nup hydrogels in previous work. We took partition and diffusion coefficients from tables in references or calculated them using concentration plots. We determined the dissociation constant K_D from the partition coefficient of the binding species (P_B) and non-binding species (P_N) and the Nup concentration N_t using $K_D = (P_B/P_I)N_t$. Note that the measured P_B is an underestimate of the true partition coefficient. We estimated the bound diffusion coefficient from the in-gel (effective) diffusion coefficient (D_{eff}) and the probability of the binding species being bound ($p_b = 1 - K_D/N_t$) using $D_B = p_b D_{\text{eff}}$. We used the reaction-diffusion equations discussed in the main text to estimate the selectivity. Because partition coefficient estimates were lower bounds, we also calculated selectivity assuming that the reported partition coefficients were 10% of their actual value. * P - Nsp1 (274-601) - P refers to a fusion between Nsp1 (274-601) and a pentameric coiled-coil P which facilitates the aggregation of the Nsp1 domain into hydrogels. See [120].

Nup fragment	Nup concentration	Molecule	MW	Partition coeff.	Diffusion coeff. in gel	Diffusion coeff. free	K_D	D_B	D_B/D_F	S	S with 10x partition coeff.	Notes
Nsp1 (2-601)	3 mM	IBB-MBP-mEGFP-ImpB MBP-mCherry	510 kD 70 kD	100 0.16	0.17 μm^2/s	4.03 μm^2/s	4.8 μM	0.17 μm^2/s	0.04	42	50	[121]
Nup57 (1-223)– Nup49 (1-246)	3.7 mM	IBB-MBP-mEGFP-ImpB MBP-mCherry	510 kD 70 kD	400 0.15	0.1 μm^2/s	2.7 μm^2/s	1.4 μM	0.1 μm^2/s	0.04	69	45	[121]
Nup57 (1-223) –Nsp1 (2-601)– Nup49 (1-246)	1.7 mM	IBB-MBP-mEGFP-ImpB MBP-mCherry	510 kD 70 kD	350 0.1	0.24 μm^2/s	4.03 μm^2/s	0.48 μM	0.24 μm^2/s	0.06	38	16	[121]
Nsp1 (2-175)	3.0 mM	IBB-MBP-mEGFP-ImpB MBP-mCherry	510 kD 70 kD	100 3	0.04 μm^2/s	12.1 μm^2/s	90 μM	0.04 μm^2/s	0.003	1.4	4.3	[122]
Nsp1 (2-601)	3.0 mM	IBB-MBP-mEGFP-ImpB MBP-mCherry	510 kD 70 kD	60 0.4	0.22 μm^2/s	6.94 μm^2/s	20 μM	0.22 μm^2/s	0.03	15	40	[122]
Nsp1 (1-601)	2.2 mM	IBB-Redstar-ImpB IBB-Redstar	530 kD 150 kD	1000 0.3	0.1 μm^2/s	0.2 μm^2/s	0.66 μM	0.1 μm^2/s	0.5	230	100	[112]
Nsp1 (1-601)	2.2 mM	GFP-ImpB IBB-Redstar	124 kD 150 kD	100 0.3	0.1-0.2 μm^2/s	0.2 μm^2/s	6.6 μM	0.1-0.2 μm^2/s	0.5-1	210-250	230-240	[112]
Nsp1 (1-601)	2.2 mM	GFP-ImpB acRedStar	124 kD 117 kD	100 0.05	0.1-0.2 μm^2/s	0.2-1 μm^2/s	1.1 μM	0.1-0.2 μm^2/s	0.1-1	94-260	53-130	[112]
P - Nsp1 (274-601) - P *	4.4 mM	IBB-MBP-mEGFP-ImpB IBB-MBP-mEGFP	510 kD 100 kD	7 0.9	2.78 μm^2/s	16.0 μm^2/s	560μM	2.42 μm^2/s	0.15	5.3	25	[120]

Our result that bound-state diffusion is required for selective transport raises a mechanistic question: how can TFs move while bound to FG Nups? Here we consider two experimentally based mechanisms: movement of the bound TF due to the intrinsic flexibility of the FG Nups [123] and multivalent binding that allows hopping of TFs between neighboring Nups [47].

Figure 4.1: (A) Schematic of the flexible tether model of bound-state diffusion. FG Nups are treated as entropic springs that constrain the motion of TFs more (top and center left, longer FG Nup) or less (top and center right, shorter Nup), which corresponds to changing width of the harmonic potential well (lower). (B) Ratio of bound to free diffusion coefficient as a function of dissociation constant, with varying polymer length in the tethered-diffusion model. (C) Selectivity as a function of K_D, with varying polymer length in the tethered-diffusion model.
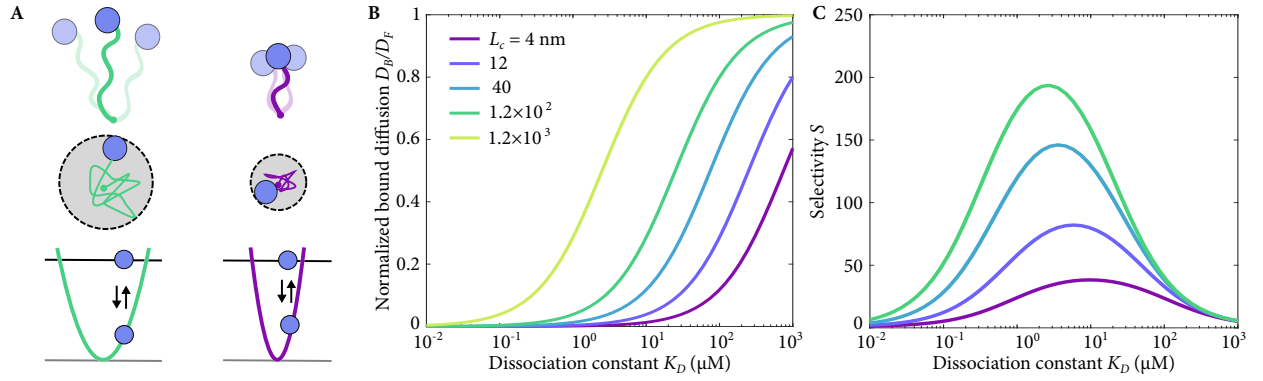
4.1.1 FG Nup flexibility allows tethered diffusion

Previous measurements have found that FG Nups are flexible and dynamic [46, 124, 125]. Although FG Nups are attached at one end to the inner surface of the NPC scaffold, chain flexibility allows a TF bound far from the tethered end to move. Flexible polymers behave as entropic springs [126] if they are not highly stretched. Therefore, a bound TF diffuses while attached to a spring-like tether, which can be represented as diffusion in a harmonic potential well (Figure 4.1A). The width of the harmonic well is related to the effective length of the flexible domain: if FG Nups are not crosslinked, the effective length is the full FG Nup length, while if they are crosslinked or entangled, the length is reduced [94]. The probability density of a TF that binds to the center of a well at $x = 0$ is $P(x,t) = e^{-\frac{x^2}{2\alpha(t)}}/\sqrt{2\pi\alpha(t)}$, where $\alpha(t) = (1 - e^{-2kD_F\beta t})/(k\beta)$, k is the spring constant of FG Nup tethering and $1/\beta = k_BT$ is the thermal energy [26]. The TF mean-squared displacement (MSD) is then $\langle x^2(t) \rangle = \int_{-\infty}^{\infty} P(x,t)x^2 dx = \alpha(t)$. The typical TF MSD during a binding event can be determined from the probability density of binding time $\rho(t) = \exp(-t/\tau)/\tau$, where $\tau = 1/k_{\text{off}}$ is the mean bound lifetime:

$$\overline{\langle x^2 \rangle} = \int_0^\infty \rho(t')\langle x^2(t')\rangle dt' = \frac{2D_F L_c \ell_p}{L_c \ell_p k_{\text{off}} + 3D_F}. \tag{4.1}$$

Here we assume that the spring constant is that of a worm-like chain polymer $k = 3/(2\beta L_c \ell_p)$, where L_c is the contour length and ℓ_p the persistence length [126].

Because FG-TF interactions have fast binding kinetics [46, 89], we estimate the bound diffusion coefficient by averaging over many binding events, while considering only bound motion, giving (Appx. C.3)

$$D_B \approx \frac{\overline{\langle x^2 \rangle}}{2\tau} = \frac{D_F L_c \ell_p k_{\text{off}}}{L_c \ell_p k_{\text{off}} + 3D_F} = \frac{D_F}{1 + 3\frac{D_F}{D_P}}. \tag{4.2}$$

Here $D_P = L_c \ell_p k_{\text{off}}$ controls the bound-state diffusion coefficient: higher D_P corresponds to a lower constraint of the TF by the tether and greater bound mobility. Bound mobility increases with increasing chain length, flexibility of the polymer, or decreasing binding lifetime. When D_P is large ($D_F/D_P \ll 1$), D_B approaches D_F, since the long, flexible chains barely affect TF motion during the short binding event. For small D_P ($D_F/D_P \gg 1$), TF motion is inhibited by a short

tether, giving $D_B \approx D_P/3 \ll D_F$. This result highlights that the kinetics of TF-FG Nup interaction are a primary determinant of the bound mobility: the faster the binding kinetics, the higher the bound diffusion constant.

Flexible disordered proteins typically have low persistence lengths [127], so we estimate $\ell_p \approx 1$ nm. If the on-rate constant is diffusion limited, $k_{on} = 10^{-3} \mu M^{-1} \mu s^{-1}$ [46, 89], the binding affinity determines the off rate. Disordered FG Nups have $L_c \approx 100$–280 nm (250–700 amino acids long [123] with a contour length per amino acid ≈ 0.4 nm). For our conservative parameters, tethered diffusion alone predicts significant selectivity $\sim$200.

4.1.2 Inter-chain hopping increases selectivity

Figure 4.2: (A) Examples of mean-squared displacement (MSD) of a simulated TF in the inter-chain hopping model, with varying hopping rate. (B) Examples of MSD distributions $\rho_{MSD}(t)$ used in estimating the diffusion coefficient, with varying unbinding rate. Tethers have 40 nm contour length; other parameters are as discussed in the main text.
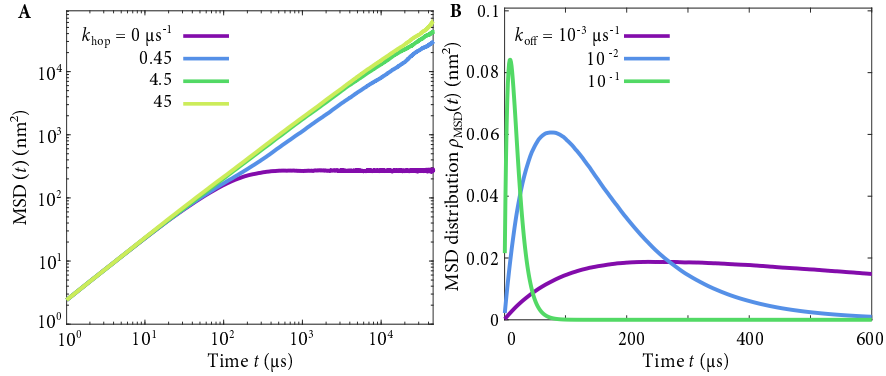
The tethered diffusion mechanism is constrained by a trade-off: tighter binding increases the TF concentration in the pore, but hinders motion. Multivalent TF-FG interactions can relax this constraint, because a TF can bind simultaneously to more than one FG Nup, moving hand-over-hand while remaining bound [128]. Consistent with this, TFs may slide between nearby FG sites rather than fully unbinding and re-binding [47]. If the newly-bound FG repeat is on a neighboring chain, the FG tether site that constrains TF motion moves while the TF remains bound. We model inter-chain hopping with a TF that undergoes tethered diffusion when bound to an FG Nup

Figure 4.3: (A) Schematic of the inter-chain hopping model of bound-state diffusion. FG Nups are treated as entropic springs that constrain the motion of TFs, and inter-chain hopping allows a TF to move from one FG Nup (top and center left, green Nup) to another (top and center right, red Nup) without unbinding, which corresponds to switching from one harmonic potential well to another (lower). (B) Ratio of bound to free diffusion coefficient as a function of dissociation constant, with varying hopping rate in the inter-chain hopping model. (C) Selectivity as a function of K_D with varying hopping rate. FG Nup contour length $L_c = 40$ nm in (B, C).

Figure 4.4: Bound diffusion and selectivity as a function of dissociation constant, with varying hopping rate for FG Nups with $L_c = 4$ nm.
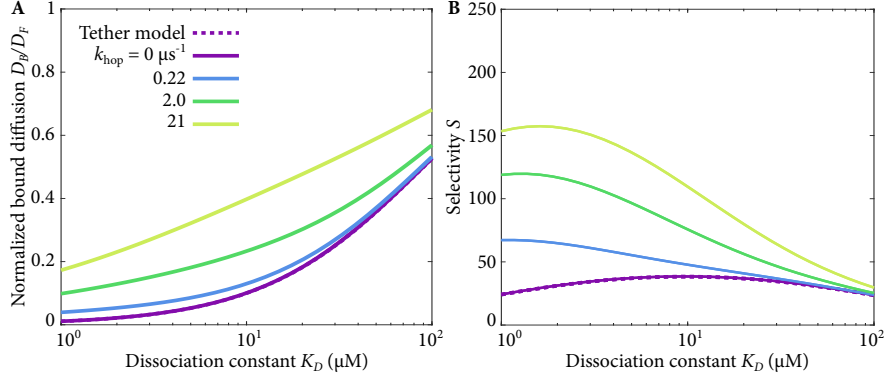
and hops between neighboring, randomly distributed tethers Figure 4.3. Numerical simulations of this model determined the bound diffusion coefficient (Figures 4.2, Appx. C.4). The Brownian dynamic simulations were done by collaborator Laura Maguire. We note that intra-chain hopping does not change the flux, since the anchor point of the tethering chain is not changed; therefore we neglect it.

Inter-chain hopping increases selectivity most for tight binding and short chains, the parameter regime where tethered diffusion gives limited selectivity (Figures 4.3, 4.4, 4.5). Hopping may therefore be important for FGs that form transient crosslinks: if FG Nups are highly crosslinked, our model suggests that inter-chain hopping is the key mechanism of TF movement. For weaker binding and longer chains, inter-chain hopping leads to a modest increase in selectivity.

4.2   Discussion

A key puzzle of the NPC is how transport-factor binding allows rapid transport through the pore. Binding typically immobilizes the bound particle, and so the increase in concentration resulting from binding does not, in general, result in increased flux. The biophysical theory we developed includes diffusion of TFs due to thermal fluctuations, binding to polymeric tethers, and the hopping of bound species between these tethers. Thus we identified principles of selective transport resulting from binding (Figure 3.1), emphasizing that bound-state mobility is essential for
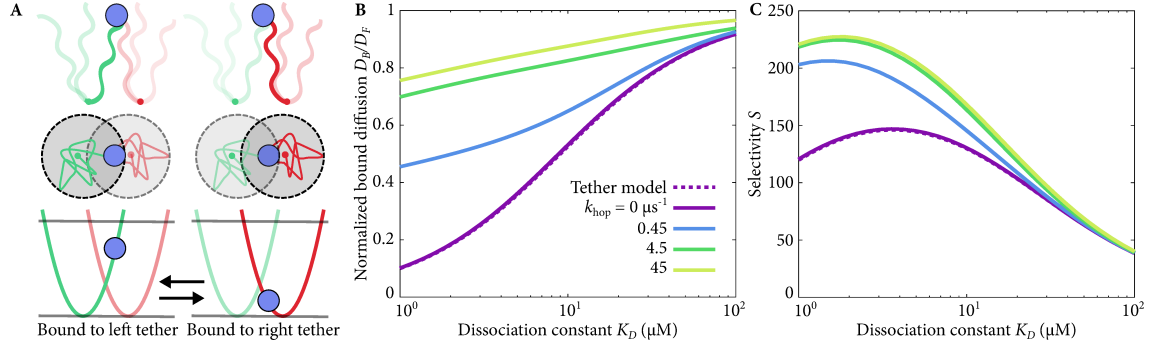
Figure 4.5: Bound diffusion and selectivity as a function of dissociation constant, with varying hopping rate for FG Nups with $L_c = 12$ nm.
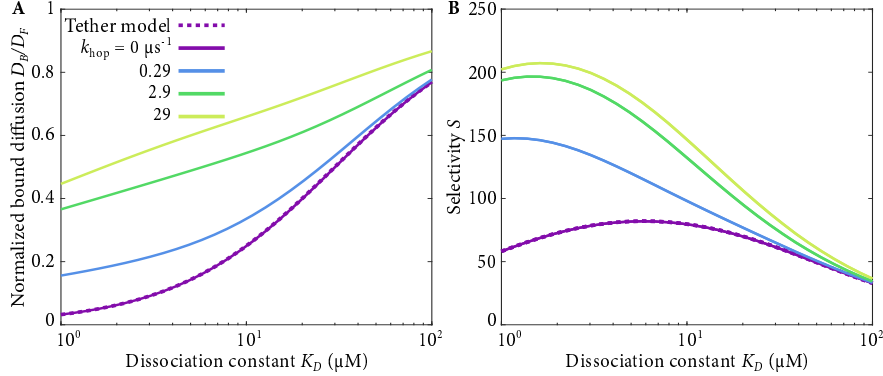

selective transport (Figure 3.2). Binding increases the local concentration, and any bound mobility increases the flux. We characterized two mechanisms to obtain bound-state mobility and found that thermally-driven diffusion of TFs bound to flexible tethers and rapid binding kinetics [46, 89] allow TF mobility, leading to selectivity similar to that observed experimentally Figure 4.1. In addition, tether flexibility enables multivalent bound particles to hop between binding regions Figure 4.3 [104, 116], further enhancing selectivity. Mobility of bound or partitioned molecules occurs in many biological contexts, suggesting that the mechanisms we study here may be broadly applicable [21, 129].

Our model for selective transport by tethered diffusion generalizes to a range of FG-FG interactions [113], if we decrease the effective chain length L_c for cohesive FG Nups. For short chains the selectivity simply due to chain flexibility is modest, suggesting that other mechanisms, like hopping, may be important. Our model suggests that transient cross-linking of FG repeats proposed to occur within the pore may serve to increase the viscosity and therefore the selectivity. Crosslinks need not be actively melted by TFs to enhance selectivity (Figure 3.5).

Our model provides a quantitative tool to evaluate selective transport. Materials formed *in vitro* by spontaneous self-assembly of FG Nups [112] or transient crosslinking by alpha-helical peptides [120] show strong selective *entry*. Using published data, we predicted whether these gels also showed selective *transport* (Table 4.1). Most synthetic gels are predicted to have $S < 10$,

Figure 4.6: Bound diffusion and selectivity as a function of dissociation constant, with varying hopping rate for FG Nups with $L_c = 120$ nm.
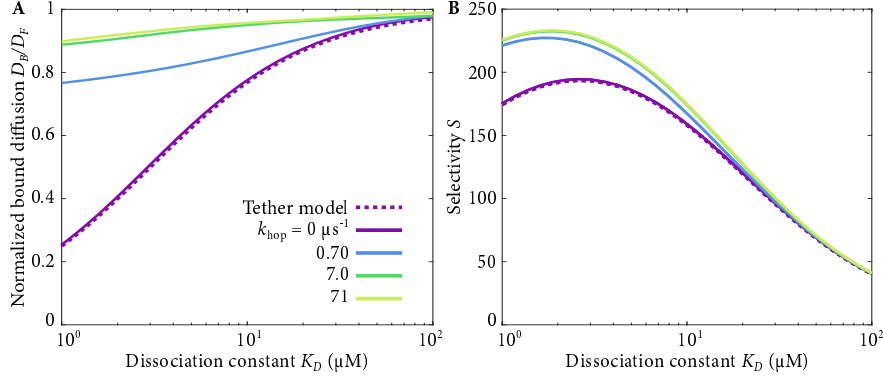

less than the selectivity of NTF2 in cells (Table 3.1). The predicted selectivity of one hydrogel is $S \approx 200$, apparently the most selective synthetic gel to date [112].

4.2.1 Overcoming the limitations of binding

Binding, even in the presence of bound-state motion, limits selectivity. Biological systems appear to have developed strategies to avoid this, for example, by using true partitioning. Lipid domains in complex membranes partition proteins [130]. Membraneless organelles spontaneously assembled from low-complexity proteins and nucleic acids can localize a molecule without immobilizing it [131]. Because membraneless organelles are fluid, the constraints imposed in our NPC model by binding are released. Our work thereby suggests a benefit of phase-separated droplets to cells: they provide significantly higher selectivity than can occur with immobilizing binding. This may be especially important for spatially complex assemblies [132].

Though we show it is not necessary, the active dissolution of polymeric biomaterials has been proposed to occur in the NPC [94]. This strategy is used by *Helicobacter pylori* to penetrate the gastric mucus [133]. Because the particularly dense extracellular matrix of solid tumors blocks the motion of particles, especially larger nanoparticles, ECM dissolution has been used to enhance drug delivery [134]. Unfortunately, this approach may not be universally applicable: breaking down the ECM surrounding tumors may promote cancer metastasis [135].

4.2.2   Design principles of selective transport by binding

Filtering by polymeric biomaterials occurs in many systems for particles of different sizes: for example, nutrients reach our intestinal walls while larger molecules are excluded. However, controlling the selective transport of similarly-sized molecules by tuning specific interactions has proven elusive. In drug delivery applications, inert nanoparticles are typically more effective at penetrating extracellular spaces and reaching their cellular targets [1]. Because biopolymer filters are the first point of contact of nanoparticles used for drug delivery, specific targeting of transport through mucus may enhance the effectiveness of drug delivery. If NPC-like bound mobility as described in our model could be achieved in these systems, it would increase the rates of transport and drug delivery.

Bibliography

[1] Jacob Witten and Katharina Ribbeck. The particle in the spider's web: Transport through biological hydrogels. Nanoscale, 9(24):8080–8095, June 2017.

[2] Felix Höfling and Thomas Franosch. Anomalous transport in the crowded world of biological cells. Rep. Prog. Phys., 76(4):046602, 2013.

[3] G J Schütz, H Schindler, and T Schmidt. Single-molecule microscopy on model membranes reveals anomalous diffusion. Biophys J, 73(2):1073–1080, August 1997.

[4] Gerhard J. Schütz, Gerald Kada, Vassili Ph. Pastushenko, and Hansgeorg Schindler. Properties of lipid microdomains in a muscle cell membrane visualized by single molecule microscopy. EMBO J, 19(5):892–901, March 2000.

[5] Dan V. Nicolau, John F. Hancock, and Kevin Burrage. Sources of Anomalous Diffusion on Cell Membranes: A Monte Carlo Study. Biophysical Journal, 92(6):1975–1987, March 2007.

[6] Aubrey V. Weigel, Blair Simon, Michael M. Tamkun, and Diego Krapf. Ergodic and non-ergodic processes coexist in the plasma membrane as observed by single-molecule tracking. PNAS, 108(16):6438–6443, April 2011.

[7] Matti Javanainen, Henrik Hammaren, Luca Monticelli, Jae-Hyung Jeon, Markus S. Miettinen, Hector Martinez-Seara, Ralf Metzler, and Ilpo Vattulainen. Anomalous and normal diffusion of proteins and lipids in crowded lipid membranes. Faraday Discuss., 161(0):397–417, 2013.

[8] Diego Krapf. Mechanisms Underlying Anomalous Diffusion in the Plasma Membrane. Curr. Top. Membr., 75:167–207, January 2015.

[9] Jae-Hyung Jeon, Matti Javanainen, Hector Martinez-Seara, Ralf Metzler, and Ilpo Vattulainen. Protein Crowding in Lipid Bilayers Gives Rise to Non-Gaussian Anomalous Lateral Diffusion of Phospholipids and Proteins. Phys. Rev. X, 6(2), April 2016.

[10] Sanaz Sadegh, Jenny L. Higgins, Patrick C. Mannion, Michael M. Tamkun, and Diego Krapf. Plasma Membrane is Compartmentalized by a Self-Similar Cortical Actin Meshwork. Phys. Rev. X, 7(1):011031, March 2017.

[11] Stella Stylianidou, Nathan J. Kuwada, and Paul A. Wiggins. Cytoplasmic Dynamics Reveals Two Modes of Nucleoid-Dependent Mobility. Biophys. J., 107(11):2684–2692, December 2014.

[12] He-Peng Zhang, Avraham Be'er, E.-L. Florin, and Harry L. Swinney. Collective motion and density fluctuations in bacterial colonies. Proc. Natl. Acad. Sci., 107(31):13626–13630, 2010.

[13] Luis H. Cisneros, John O. Kessler, Sujoy Ganguly, and Raymond E. Goldstein. Dynamics of swimming bacteria: Transition to directional order at high concentration. Phys. Rev. E, 83(6):061907, June 2011.

[14] Shashi Thutupalli, Mingzhai Sun, Filiz Bunyak, Kannappan Palaniappan, and Joshua W. Shaevitz. Directional reversals enable Myxococcus xanthus cells to produce collective one-dimensional streams during fruiting-body formation. J. R. Soc. Interface, 12(109):20150049, August 2015.

[15] M. C. Marchetti, J. F. Joanny, S. Ramaswamy, T. B. Liverpool, J. Prost, Madan Rao, and R. Aditi Simha. Hydrodynamics of soft active matter. Rev. Mod. Phys., 85(3):1143–1189, July 2013.

[16] Robert Zwanzig. Nonequilibrium Statistical Mechanics. Oxford University Press, Oxford ; New York, 2001.

[17] A. Einstein. Über die von der molekularkinetischen Theorie der Wärme geforderte Bewegung von in ruhenden Flüssigkeiten suspendierten Teilchen. Ann. Phys., 322(8):549–560, January 1905.

[18] Neil W. Ashcroft and N. David Mermin. Solid State Physics. Brooks Cole, New York, 1 edition edition, January 1976.

[19] P. D. Lett, W. D. Phillips, S. L. Rolston, C. E. Tanner, R. N. Watts, and C. I. Westbrook. Optical molasses. J. Opt. Soc. Am. B, JOSAB, 6(11):2084–2107, November 1989.

[20] Howard C. Berg. Random Walks in Biology. Princeton University Press, Princeton, N.J, revised edition edition, September 1993.

[21] Michael W Stefferson, Samantha L Norris, Franck J Vernerey, Meredith D Betterton, and Loren E Hough. Effects of soft interactions and bound mobility on diffusion in crowded environments: A model of sticky and slippery obstacles. Phys. Biol., 14(4):045008, June 2017.

[22] Umberto Marini Bettolo Marconi and Pedro Tarazona. Dynamic density functional theory of fluids. J. Chem. Phys., 110(16):8032–8044, April 1999.

[23] Umberto Marini Bettolo Marconi and Pedro Tarazona. Dynamic density functional theory of fluids. J. Phys.: Condens. Matter, 12(8A):A413, 2000.

[24] A. J. Archer and R. Evans. Dynamical density functional theory and its application to spinodal decomposition. J. Chem. Phys., 121(9):4246–4254, September 2004.

[25] A J Archer. Dynamical density functional theory: Binary phase-separating colloidal fluid in a cavity. J. Phys. Condens. Matter, 17(10):1405–1427, March 2005.

[26] Masao Doi and S. F. Edwards. The Theory of Polymer Dynamics. Clarendon Press, 1988.

[27] P. S. Grassia, E. J. Hinch, and L. C. Nitsche. Computer simulations of Brownian motion of complex systems. J. Fluid Mech., 282:373–403, January 1995.

[28] Ralf Metzler and Joseph Klafter. The random walk's guide to anomalous diffusion: A fractional dynamics approach. Phys. Rep., 339(1):1–77, December 2000.

[29] Igor M. Sokolov, Joseph Klafter, and Alexander Blumen. Fractional Kinetics. Physics Today, 55(11):48–54, November 2002.

[30] M. J. Saxton. Anomalous diffusion due to obstacles: A Monte Carlo study. Biophys. J., 66(2):394–401, February 1994.

[31] T. J. Feder, I. Brust-Mascher, J. P. Slattery, B. Baird, and W. W. Webb. Constrained diffusion or immobile fraction on cell surfaces: A new interpretation. Biophys. J., 70(6):2767–2773, June 1996.

[32] Matthias Weiss, Markus Elsner, Fredrik Kartberg, and Tommy Nilsson. Anomalous Subdiffusion Is a Measure for Cytoplasmic Crowding in Living Cells. Biophys. J., 87(5):3518–3524, November 2004.

[33] R. N. Ghosh and W. W. Webb. Automated detection and tracking of individual and clustered cell surface low density lipoprotein receptor molecules. Biophys. J., 66(5):1301–1318, May 1994.

[34] M. J. Saxton. Lateral diffusion in an archipelago. The effect of mobile obstacles. Biophysical Journal, 52(6):989–997, December 1987.

[35] M. J. Saxton. Anomalous diffusion due to binding: A Monte Carlo study. Biophys. J., 70(3):1250–1262, March 1996.

[36] Adam J. Ellery, Matthew J. Simpson, Scott W. McCue, and Ruth E. Baker. Characterizing transport through a crowded environment with different obstacle sizes. The Journal of Chemical Physics, 140(5):054108, February 2014.

[37] Adam J. Ellery, Ruth E. Baker, and Matthew J. Simpson. Communication: Distinguishing between short-time non-Fickian diffusion and long-time Fickian diffusion for a random walk on a crowded lattice. J. Chem. Phys., 144(17):171104, May 2016.

[38] Adam J. Ellery, Ruth E. Baker, Scott W. McCue, and Matthew J. Simpson. Modeling transport through an environment crowded by a mixture of obstacles of different shapes and sizes. Physica A: Statistical Mechanics and its Applications, 449:74–84, May 2016.

[39] Adam J. Ellery, Ruth E. Baker, and Matthew J. Simpson. Calculating the Fickian diffusivity for a lattice-based random walk with agents and obstacles of different shapes and sizes. Phys. Biol., 12(6):066010, 2015.

[40] Adam J. Ellery, Ruth E. Baker, and Matthew J. Simpson. An analytical method for disentangling the roles of adhesion and crowding for random walk models on a crowded lattice. Phys. Biol., 13(5):05LT02, 2016.

[41] Annika Wedemeier, Ting Zhang, Holger Merlitz, Chen-Xu Wu, and Jorg Langowski. The role of chromatin conformations in diffusional transport of chromatin-binding proteins: Cartesian lattice simulations. The Journal of Chemical Physics, 128(15):155101, April 2008.

[42] Annika Wedemeier, Holger Merlitz, Chen-Xu Wu, and Jorg Langowski. Modeling diffusional transport in the interphase cell nucleus. The Journal of Chemical Physics, 127(4):045102, July 2007.

[43] Annika Wedemeier, Holger Merlitz, Wu Wu, and Jorg Langowski. How proteins squeeze through polymer networks: A Cartesian lattice study. The Journal of Chemical Physics, 131(6):064905, August 2009.

[44] Clifford P. Brangwynne, Christian R. Eckmann, David S. Courson, Agata Rybarska, Carsten Hoege, Jöbin Gharakhani, Frank Jülicher, and Anthony A. Hyman. Germline P Granules Are Liquid Droplets That Localize by Controlled Dissolution/Condensation. Science, 324(5935):1729–1732, June 2009.

[45] Amandine Molliex, Jamshid Temirov, Jihun Lee, Maura Coughlin, Anderson P. Kanagaraj, Hong Joo Kim, Tanja Mittag, and J. Paul Taylor. Phase Separation by Low Complexity Domains Promotes Stress Granule Assembly and Drives Pathological Fibrillization. Cell, 163(1):123–133, September 2015.

[46] Loren E. Hough, Kaushik Dutta, Samuel Sparks, Deniz B. Temel, Alia Kamal, Jaclyn Tetenbaum-Novatt, Michael P. Rout, and David Cowburn. The molecular mechanism of nuclear transport revealed by atomic-scale measurements. eLife, 4:e10027, September 2015.

[47] Barak Raveh, Jerome M. Karp, Samuel Sparks, Kaushik Dutta, Michael P. Rout, Andrej Sali, and David Cowburn. Slide-and-exchange mechanism for rapid and selective transport through the nuclear pore complex. PNAS, 113(18):E2489–E2497, March 2016.

[48] Benjamin L. Timney, Barak Raveh, Roxana Mironska, Jill M. Trivedi, Seung Joong Kim, Daniel Russel, Susan R. Wente, Andrej Sali, and Michael P. Rout. Simple rules for passive diffusion through the nuclear pore complex. J. Cell Biol., 215(1):57–76, September 2016.

[49] L Maguire. Design principles of binding-induced selective transport through the nuclear pore complex, 2018.

[50] Jean-Pierre Hansen and Ian R. McDonald. Theory of Simple Liquids. Elsevier Academic Press, London ; Burlington, MA, 3rd ed edition, 2006.

[51] Aparna Baskaran and M. Cristina Marchetti. Hydrodynamics of self-propelled hard rods. Phys. Rev. E, 77(1), January 2008.

[52] Aparna Baskaran and M. Cristina Marchetti. Enhanced Diffusion and Ordering of Self-Propelled Rods. Phys. Rev. Lett., 101(26), December 2008.

[53] H. H. Wensink and H. Löwen. Aggregation of self-propelled colloidal rods near confining walls. Phys. Rev. E, 78(3), September 2008.

[54] A. Baskaran and M. C. Marchetti. Self-regulation in self-propelled nematic fluids. Eur. Phys. J. E, 35(9), September 2012.

[55] Francesco Ginelli, Fernando Peruani, Markus Bär, and Hugues Chaté. Large-Scale Collective Properties of Self-Propelled Rods. Phys. Rev. Lett., 104(18):184502, May 2010.

[56] Hui-Shun Kuan, Robert Blackwell, Loren E. Hough, Matthew A. Glaser, and M. D. Betterton. Hysteresis, reentrance, and glassy dynamics in systems of self-propelled rods. Phys. Rev. E, 92(6), December 2015.

[57] Stefferson. Dynamical, 2018.

[58] J. H. Petropoulos. Membrane transport properties in relation to microscopic and macroscopic structural inhomogeneity. J. Membr. Sci., 52(3):305–323, September 1990.

[59] Sarah L. Veatch and Sarah L. Keller. Organization in Lipid Membranes Containing Cholesterol. Phys. Rev. Lett., 89(26):268101, December 2002.

[60] Peter B Crowley, Elysian Chow, and Tatiana Papkovskaia. Protein Interactions in the Escherichia coli Cytosol: An Impediment to In-Cell NMR Spectroscopy. Chembiochem, 12(7):1043–1048, 2011.

[61] Márcio A. Mourão, Joe B. Hakim, and Santiago Schnell. Connecting the Dots: The Effects of Macromolecular Crowding on Cell Physiology. Biophys. J., 107(12):2761–2766, December 2014.

[62] Vladimir P. Zhdanov and Fredrik Höök. Kinetics of enzymatic reactions in lipid membranes containing domains. Phys. Biol., 12(2):026003, April 2015.

[63] Takahiro Fujiwara, Ken Ritchie, Hideji Murakoshi, Ken Jacobson, and Akihiro Kusumi. Phospholipids undergo hop diffusion in compartmentalized cell membrane. J. Cell Biol., 157(6):1071–1082, June 2002.

[64] Martin B. Forstner, Douglas S. Martin, Florian Rückerl, Josef A. Käs, and Carsten Selle. Attractive membrane domains control lateral diffusion. Phys. Rev. E, 77(5):051906, May 2008.

[65] Jens Ehrig, Eugene P. Petrov, and Petra Schwille. Near-Critical Fluctuations and Cytoskeleton-Assisted Phase Separation Lead to Subdiffusion in Cell Membranes. Biophys. J., 100(1):80–89, January 2011.

[66] John R. Silvius. Partitioning of membrane molecules between raft and non-raft domains: Insights from model-membrane studies. Biochim. Biophys. Acta BBA - Mol. Cell Res., 1746(3):193–202, December 2005.

[67] Aditya Iyer, Nathalie Schilderink, Mireille M. A. E. Claessens, and Vinod Subramaniam. Membrane-Bound Alpha Synuclein Clusters Induce Impaired Lipid Diffusion and Increased Lipid Packing. Biophys. J., 111(11):2440–2449, December 2016.

[68] Hugues Berry. Monte carlo simulations of enzyme reactions in two dimensions: Fractal kinetics and spatial segregation. Biophys J, 83(4):1891–1901, October 2002.

[69] Daniel S. Banks and Cécile Fradin. Anomalous Diffusion of Proteins Due to Molecular Crowding. Biophys. J., 89(5):2960–2971, November 2005.

[70] Prithviraj Nandigrami, Brandy Grove, Andrew Konya, and Robin L. B. Selinger. Gradient-driven diffusion and pattern formation in crowded mixtures. Phys. Rev. E, 95(2):022107, February 2017.

[71] Jean-François Mercier and Gary W. Slater. Numerically exact diffusion coefficients for lattice systems with periodic boundary conditions. II. Numerical approach and applications. J. Chem. Phys., 110(12):6057–6065, March 1999.

[72] Jean-François Mercier, Gary W. Slater, and Hong L. Guo. Numerically exact diffusion co-efficients for lattice systems with periodic boundary conditions. I. Theory. J. Chem. Phys., 110(12):6050–6056, March 1999.

[73] A. Wedemeier, H. Merlitz, and J. Langowski. Anomalous diffusion in the presence of mobile obstacles. EPL, 88(3):38004, November 2009.

[74] Nicholas Metropolis, Arianna W. Rosenbluth, Marshall N. Rosenbluth, Augusta H. Teller, and Edward Teller. Equation of State Calculations by Fast Computing Machines. J. Chem. Phys., 21(6):1087–1092, June 1953.

[75] Marcin Magdziarz, Aleksander Weron, Krzysztof Burnecki, and Joseph Klafter. Fractional Brownian Motion Versus the Continuous-Time Random Walk: A Simple Test for Subdiffusive Dynamics. Phys. Rev. Lett., 103(18):180602, October 2009.

[76] Johannes H. P. Schulz, Eli Barkai, and Ralf Metzler. Aging Renewal Theory and Application to Random Walks. Phys. Rev. X, 4(1):011028, February 2014.

[77] M. J. Saxton. Single-particle tracking: The distribution of diffusion coefficients. Biophys. J., 72(4):1744–1753, April 1997.

[78] Dietrich Stauffer and Ammon Aharony. Introduction To Percolation Theory. Taylor & Francis, July 1994.

[79] Niels Høiby, Thomas Bjarnsholt, Michael Givskov, Søren Molin, and Oana Ciofu. Antibiotic resistance of bacterial biofilms. International Journal of Antimicrobial Agents, 35(4):322–332, April 2010.

[80] Anselm Fabian Lowell Schneider and Christian Peter Richard Hackenberger. Fluorescent labelling in living cells. Current Opinion in Biotechnology, 48:61–68, December 2017.

[81] Xinglu Huang, Jane Chisholm, Jie Zhuang, Yanyu Xiao, Gregg Duncan, Xiaoyuan Chen, Jung Soo Suk, and Justin Hanes. Protein nanocages that penetrate airway mucus and tumor tissue. Proc. Natl. Acad. Sci., 114(32):E6595–E6602, August 2017.

[82] Panagiotis Mastorakos, Adriana L. da Silva, Jane Chisholm, Eric Song, Won Kyu Choi, Michael P. Boyle, Marcelo M. Morales, Justin Hanes, and Jung Soo Suk. Highly compacted biodegradable DNA nanoparticles capable of overcoming the mucus barrier for inhaled lung gene therapy. PNAS, 112(28):8720–8725, July 2015.

[83] Stuart S. Olmsted, Janet L. Padgett, Ashley I. Yudin, Kevin J. Whaley, Thomas R. Moench, and Richard A. Cone. Diffusion of Macromolecules and Virus-Like Particles in Human Cervical Mucus. Biophysical Journal, 81(4):1930–1937, October 2001.

[84] S. K. Lai, K. Hida, S. Shukair, Y.-Y. Wang, A. Figueiredo, R. Cone, T. J. Hope, and J. Hanes. Human Immunodeficiency Virus Type 1 Is Trapped by Acidic but Not by Neutralized Human Cervicovaginal Mucus. J. Virol., 83(21):11196–11200, November 2009.

[85] Alex Chen, Scott A. McKinley, Simi Wang, Feng Shi, Peter J. Mucha, M. Gregory Forest, and Samuel K. Lai. Transient Antibody-Mucin Interactions Produce a Dynamic Molecular Shield against Viral Invasion. Biophys J, 106(9):2028–2036, May 2014.

[86] Caterina Strambio-De-Castillia, Mario Niepel, and Michael P. Rout. The nuclear pore complex: Bridging nuclear transport and gene regulation. Nat Rev Mol Cell Biol, 11(7):490–501, July 2010.

[87] Rui Zhou, Haiying Zhou, Bin Xiong, Yan He, and Edward S. Yeung. Pericellular Matrix Enhances Retention and Cellular Uptake of Nanoparticles. J. Am. Chem. Soc., 134(32):13404–13409, August 2012.

[88] Weidong Yang, Jeff Gelles, and Siegfried M. Musser. Imaging of single-molecule translocation through nuclear pore complexes. PNAS, 101(35):12887–12892, August 2004.

[89] Sigrid Milles, Davide Mercadante, Iker Valle Aramburu, Malene Ringkjøbing Jensen, Niccolò Banterle, Christine Koehler, Swati Tyagi, Jane Clarke, Sarah L. Shammas, Martin Blackledge, Frauke Gräter, and Edward A. Lemke. Plasticity of an Ultrafast Interaction between Nucleoporins and Nuclear Transport Receptors. Cell, 163(3):734–745, October 2015.

[90] Benjamin L. Timney, Jaclyn Tetenbaum-Novatt, Diana S. Agate, Rosemary Williams, Wenzhu Zhang, Brian T. Chait, and Michael P. Rout. Simple kinetic relationships and nonspecific competition govern nuclear import rates in vivo. J. Cell Biol., 175(4):579–593, November 2006.

[91] Hermann Broder Schmidt and Dirk Görlich. Nup98 FG domains from diverse species spontaneously phase-separate into particles with nuclear pore-like permselectivity. eLife Sciences, 4:e04251, January 2015.

[92] Jan Peter Siebrasse and Reiner Peters. Rapid translocation of NTF2 through the nuclear pore of isolated nuclei and nuclear envelopes. EMBO Rep., 3(9):887–892, September 2002.

[93] Nikolai I. Kiskin, Jan P. Siebrasse, and Reiner Peters. Optical Microwell Assay of Membrane Transport Kinetics. Biophysical Journal, 85(4):2311–2322, October 2003.

[94] K Ribbeck and D Görlich. Kinetic analysis of translocation through nuclear pore complexes. The EMBO Journal, 20(6):1320–1330, 2001.

[95] Stefano Pagliara, Simon L. Dettmer, and Ulrich F. Keyser. Channel-Facilitated Diffusion Boosted by Particle Binding at the Channel Entrance. Phys. Rev. Lett., 113(4), July 2014.

[96] Anton Zilman, Stefano Di Talia, Brian T. Chait, Michael P. Rout, and Marcelo O. Magnasco. Efficiency, Selectivity, and Robustness of Nucleocytoplasmic Transport. PLOS Computational Biology, 3(7):e125, July 2007.

[97] Mario Tagliazucchi, Orit Peleg, Martin Kröger, Yitzhak Rabin, and Igal Szleifer. Effect of charge, hydrophobicity, and sequence of nucleoporins on the translocation of model particles through the nuclear pore complex. PNAS, 110(9):3363–3368, February 2013.

[98] Li-Chun Tu, Guo Fu, Anton Zilman, and Siegfried M. Musser. Large cargo transport by nuclear pores: Implications for the spatial organization of FG-nucleoporins. EMBO J., 32(24):3220–3230, December 2013.

[99] Lisa A Strawn, Tianxiang Shen, Nataliya Shulga, David S Goldfarb, and Susan R Wente. Minimal nuclear pore complexes define FG repeat domains essential for transport. Nat Cell Biol, 6(3):197–206, 2004. PMID: 15039779.

[100] Bryan Zeitler and Karsten Weis. The FG-repeat asymmetry of the nuclear pore complex is dispensable for bulk nucleocytoplasmic transport in vivo. J Cell Biol, 167(4):583–590, November 2004.

[101] Stefan W. Kowalczyk, Larisa Kapinos, Timothy R. Blosser, Tomás Magalhães, Pauline van Nies, Roderick Y. H. Lim, and Cees Dekker. Single-molecule transport across an individual biomimetic nuclear pore complex. Nat Nano, 6(7):433–438, July 2011.

[102] Tijana Jovanovic-Talisman, Jaclyn Tetenbaum-Novatt, Anna Sophia McKenney, Anton Zilman, Reiner Peters, Michael P Rout, and Brian T Chait. Artificial nanopores that mimic the transport selectivity of the nuclear pore complex. Nature, 457(7232):1023–1027, 2009.

[103] K Ribbeck, G Lipowsky, H M Kent, M Stewart, and D Görlich. NTF2 mediates nuclear import of Ran. The EMBO Journal, 17(22):6587–6598, 1998.

[104] Alan R. Lowe, Jeffrey H. Tang, Jaime Yassif, Michael Graf, William Y. C. Huang, Jay T. Groves, Karsten Weis, and Jan T. Liphardt. Importin-β modulates the permeability of the nuclear pore complex in a Ran-dependent manner. eLife Sciences, page e04052, March 2015.

[105] Daphna Frenkiel-Krispin, Bohumil Maco, Ueli Aebi, and Ohad Medalia. Structural Analysis of a Metazoan Nuclear Pore Complex Reveals a Fused Concentric Ring Architecture. Journal of Molecular Biology, 395(3):578–586, January 2010.

[106] Joshua S Mincer and Sanford M Simon. Simulations of nuclear pore transport yield mechanistic insights and quantitative predictions. P Natl Acad Sci Usa, 108(31):E351–8, 2011.

[107] D. Görlich, N. Panté, U. Kutay, U. Aebi, and F. R. Bischoff. Identification of different roles for RanGDP and RanGTP in nuclear protein import. The EMBO Journal, 15(20):5584–5594, October 1996.

[108] Daniel Gilchrist, Brook Mykytka, and Michael Rexach. Accelerating the Rate of Disassembly of Karyopherin·Cargo Complexes. J. Biol. Chem., 277(20):18161–18172, May 2002.

[109] Gregory Riddick and Ian G Macara. A systems analysis of importin-alpha-beta-mediated nuclear protein import. J Cell Biol, 168(7):1027–1038, 2005.

[110] Malik Juweid, Ronald Neumann, Chaing Paik, Miguel J. Perez-Bacete, Jun Sato, William van Osdol, and John N. Weinstein. Micropharmacology of Monoclonal Antibodies in Solid Tumors: Direct Experimental Evidence for a Binding Site Barrier. Cancer Res, 52(19):5144–5153, October 1992.

[111] Michael P. Rout, John D. Aitchison, Adisetyantari Suprapto, Kelly Hjertaas, Yingming Zhao, and Brian T. Chait. The Yeast Nuclear Pore Complex Composition, Architecture, and Transport Mechanism. J Cell Biol, 148(4):635–652, February 2000.

[112] Steffen Frey and Dirk Görlich. A Saturated FG-Repeat Hydrogel Can Reproduce the Permeability Properties of Nuclear Pore Complexes. Cell, 130(3):512–523, August 2007.

[113] Andrei Vovk, Chad Gu, Michael G. Opferman, Larisa E. Kapinos, Roderick YH Lim, Rob D. Coalson, David Jasnow, and Anton Zilman. Simple biophysics underpins collective conformations of the intrinsically disordered proteins of the Nuclear Pore Complex. eLife Sciences, 5:e10785, May 2016.

[114] Justin Yamada, Joshua L Phillips, Samir Patel, Gabriel Goldfien, Alison Calestagne-Morelli, Hans Huang, Ryan Reza, Justin Acheson, Viswanathan V Krishnan, Shawn Newsam, Ajay Gopinathan, Edmond Y Lau, Michael E Colvin, Vladimir N Uversky, and Michael F Rexach. A bimodal distribution of two distinct categories of intrinsically disordered structures with separate functions in FG nucleoporins. Molecular & Cellular Proteomics, 9(10):2205–2224, 2010.

[115] David Ando, Roya Zandi, Yong Woon Kim, Michael Colvin, Michael Rexach, and Ajay Gopinathan. Nuclear Pore Complex Protein Sequences Determine Overall Copolymer Brush Structure and Function. Biophysical Journal, 106(9):1997–2007, May 2014.

[116] Rafael L. Schoch, Larisa E. Kapinos, and Roderick Y. H. Lim. Nuclear transport receptor binding avidity triggers a self-healing collapse transition in FG-nucleoporin molecular brushes. PNAS, 109(42):16911–16916, October 2012.

[117] Joan Pulupa, Manas Rachh, Michael D. Tomasini, Joshua S. Mincer, and Sanford M. Simon. A coarse-grained computational model of the nuclear pore complex predicts Phe-Gly nucleoporin dynamics. J. Gen. Physiol., page jgp.201711769, September 2017.

[118] J Tetenbaum-Novatt and M P Rout. The mechanism of nucleocytoplasmic transport through the nuclear pore complex. Cold Spring Harb. Symp. Quant. Biol., 75:567–584, 2010.

[119] Thomas Bickel and Robijn Bruinsma. The nuclear pore complex mystery and anomalous diffusion in reversible gels. Biophys. J., 83(6):3079–3087, 2002.

[120] Jaeyun Kim, Weiwei Aileen Li, Youngjin Choi, Sarah A. Lewin, Catia S. Verbeke, Glenn Dranoff, and David J. Mooney. Injectable, spontaneously assembling inorganic scaffolds modulate immune cells in vivo and increase vaccine efficacy. Nat Biotechnol, 33(1):64–72, January 2015.

[121] Steffen Frey and Dirk Görlich. FG/FxFG as well as GLFG repeats form a selective permeability barrier with self-healing properties. The EMBO Journal, 28(17):2554–2567, 2009.

[122] C Ader, S Frey, W Maas, H B Schmidt, D Gorlich, and M Baldus. Amyloid-like interactions within nucleoporin FG hydrogels. Proceedings of the National Academy of Sciences, pages 1–5, 2010.

[123] Samir S Patel, Brian J Belmont, Joshua M Sante, and Michael F Rexach. Natively unfolded nucleoporins gate protein diffusion across the nuclear pore complex. Cell, 129(1):83–96, 2007.

[124] Roderick Y. H. Lim, Birthe Fahrenkrog, Joachim Köser, Kyrill Schwarz-Herion, Jie Deng, and Ueli Aebi. Nanomechanical Basis of Selective Gating by the Nuclear Pore Complex. Science, 318(5850):640–643, October 2007.

[125] Sigrid Milles and Edward A. Lemke. Mapping Multivalency and Differential Affinities within Large Intrinsically Disordered Protein Complexes with Segmental Motion Analysis. Angew. Chem. Int. Ed., 53(28):7364–7367, July 2014.

[126] Jonathon Howard. Mechanics of Motor Proteins and the Cytoskeleton. Sinauer Associates, Publishers, Sunderland, Mass, 2001.

[127] Véronique Receveur-Bréchot and Dominique Durand. How Random are Intrinsically Disordered Proteins? A Small Angle Scattering Perspective. Curr Protein Pept Sci, 13(1):55–75, February 2012.

[128] Jaclyn Tetenbaum-Novatt, Loren E Hough, Roxana Mironska, Anna Sophia McKenney, and Michael P Rout. Nucleocytoplasmic transport: A role for non-specific competition in karyopherin-nucleoporin interactions. Mol Cell Proteomics, 2012.

[129] José Braga, James G. McNally, and Maria Carmo-Fonseca. A Reaction-Diffusion Model to Study RNA Motion by Quantitative Fluorescence Recovery after Photobleaching. Biophysical Journal, 92(8):2694–2703, April 2007.

[130] Kai Simons and Julio L. Sampaio. Membrane Organization and Lipid Rafts. Cold Spring Harb Perspect Biol, 3(10), October 2011.

[131] Clifford P. Brangwynne, Peter Tompa, and Rohit V. Pappu. Polymer physics of intracellular phase transitions. Nat Phys, 11(11):899–904, November 2015.

[132] Marina Feric, Nilesh Vaidya, Tyler S. Harmon, Diana M. Mitrea, Lian Zhu, Tiffany M. Richardson, Richard W. Kriwacki, Rohit V. Pappu, and Clifford P. Brangwynne. Coexisting Liquid Phases Underlie Nucleolar Subcompartments. Cell, 165(7):1686–1697, June 2016.

[133] Jonathan P. Celli, Bradley S. Turner, Nezam H. Afdhal, Sarah Keates, Ionita Ghiran, Ciaran P. Kelly, Randy H. Ewoldt, Gareth H. McKinley, Peter So, and Shyamsunder Erramilli. Helicobacter pylori moves through mucus by reducing mucin viscoelasticity. Proc. Natl. Acad. Sci., 106(34):14321–14326, 2009.

[134] Yan Zhou and Jindřich Kopeček. Biological rationale for the design of polymeric anti-cancer nanomedicines. J. Drug Target., 21(1):1–26, January 2013.

[135] Lei Miao, C. Michael Lin, and Leaf Huang. Stromal barriers and strategies for the delivery of nanomedicine to desmoplastic tumors. J. Controlled Release, 219:192–204, December 2015.

[136] Andrew J Archer and Markus Rauscher. Dynamical density functional theory for interacting Brownian particles: Stochastic or deterministic? J. Phys. Math. Gen., 37(40):9325–9333, October 2004.

[137] R. Evans. The nature of the liquid-vapour interface and other topics in the statistical mechanics of non-uniform, classical fluids. Adv. Phys., 28(2):143–200, April 1979.

[138] Carmine Di Rienzo, Vincenzo Piazza, Enrico Gratton, Fabio Beltram, and Francesco Cardarelli. Probing short-range protein Brownian motion in the cytoplasm of living cells. Nat. Commun., 5:5891, December 2014.

[139] James A. Dix and A. S. Verkman. Crowding Effects on Diffusion in Solutions and Cells. Annu. Rev. Biophys., 37(1):247–263, 2008.

[140] Surya K. Ghosh, Andrey G. Cherstvy, and Ralf Metzler. Non-universal tracer diffusion in crowded media of non-inert obstacles. Phys Chem Chem Phys, 17(3):1847–1858, 2015.

[141] Hugues Berry and Hugues Chaté. Anomalous diffusion due to hindering by mobile obstacles undergoing Brownian motion or Orstein-Ulhenbeck processes. Phys. Rev. E, 89(2):022708, February 2014.

[142] Tal Maimon, Nadav Elad, Idit Dahan, and Ohad Medalia. The Human Nuclear Pore Complex as Revealed by Cryo-Electron Tomography. Structure, 20(6):998–1006, June 2012.

[143] Francesco Cardarelli and Enrico Gratton. In Vivo Imaging of Single-Molecule Translocation Through Nuclear Pore Complexes by Pair Correlation Functions. PLOS ONE, 5(5):e10475, May 2010.

[144] Brook Pyhtila and Michael Rexach. A gradient of affinity for the karyopherin Kap95p along the yeast nuclear pore complex. J Biol Chem, 278(43):42699–42709, 2003.

[145] Robert Blackwell, Christopher Edelmaier, Oliver Sweezy-Schindler, Adam Lamson, Zachary R. Gergely, Eileen O'Toole, Ammon Crapo, Loren E. Hough, J. Richard McIntosh, Matthew A. Glaser, and Meredith D. Betterton. Physical determinants of bipolar mitotic spindle assembly and stability in fission yeast. Sci. Adv., 3(1):e1601603, January 2017.

Appendix A

Fluctuation-dissipation theorem

Here, we will derive the fluctuation-dissipation theorem which will connect the drag force and random fluctuating force for a particle in a heat bath. The derivation closely follows Ref. [16]. Let us start with the Langevin equation in one dimension,

$$\dot{v} = -\frac{1}{m}\left[\zeta v + -\frac{\partial U}{\partial x} + \xi(t)\right], \tag{A.1}$$

where m is the mass of the particle, ζ is the drag, U is the potential energy, and ξ is random fluctuating force. For a non-interacting Brownian particle in the absence of external fields,

$$\dot{v} = -\frac{1}{m}\left[\zeta v + \xi(t)\right]. \tag{A.2}$$

The random force is zero on average (no preferred direction), there are no correlations between random kicks in time (all kicks are independent events), and there is some unknown constant amplitude of these forces. We can expressed these features as

$$\langle \xi(t) \rangle = 0 \qquad \langle \xi(t)\xi(t') \rangle = C\delta(t - t'), \tag{A.3}$$

where C is the unknown coefficient. The brackets $\langle ... \rangle$ describe a ensemble average of the noise— *i.e.*, an average over all realizations. We can think of each kick as sampling some noise distribution with the properties given in Eqn. A.3. To solve for C, let's solve for the velocity as a function of time. To solve the linear ordinary differential equation, let $v(t) = e^{-\zeta t/m}y(t)$. This gives

$$\dot{y} = e^{\zeta t/m}\frac{\xi(t)}{m}, \tag{A.4}$$

which can be integrated to

$$y(t) = y(0) + \int_0^t e^{\zeta t'/m} \frac{\xi(t')}{m} dt'.$$

(A.5)

Returning to the velocity we get

$$v(t) = e^{-\zeta t/m} \left[v(0) + \frac{1}{m} \int_0^t e^{\zeta t'/m} \xi(t') dt' \right].$$

(A.6)

Now, we can solve for the noise average velocity squared by Eqn. A.6 and taking the ensemble averaged

$$
\begin{aligned}
\langle v(t)^2 \rangle &= e^{2\zeta t/m} \left[v(0)^2 + \frac{v(0)}{m} \int_0^t e^{\zeta t'/m} \langle \xi(t') \rangle dt' \right. \\
&\quad \left. + \frac{1}{m^2} \int_0^t \int_0^t e^{\zeta(s'+t')/m} \langle \xi(t')\xi(s') \rangle ds' dt' \right] \\
&= e^{-2\zeta t/m} \left[v(0)^2 + \frac{C}{m^2} \int_0^t e^{2\zeta t'/m} dt' \right] \\
&= e^{-2\zeta t'/m} v(0)^2 + \frac{C}{2\zeta m} \left[1 - e^{2\zeta t/m} \right].
\end{aligned}
$$

(A.7)

From the equipartition theorem, $\frac{1}{2}mv^2 = \frac{1}{2}k_B T$. Thus, as $t \to \infty$, the particle will thermalize and equilibrate. By plugging Eqn. A.7 into the equipartition theorem and taking the late time limit, we get fluctuation-dissipation theorem:

$$C = 2\zeta k_B T.$$

(A.8)

For completeness, let's summarize the results as,

$$\langle \xi(t) \rangle = 0 \qquad \langle \xi(t)\xi(t') \rangle = 2\zeta k_B T \delta(t - t').$$

(A.9)

The fluctuation-dissipation connects the random force fluctuation amplitude to the drag force through ζ.

Appendix B

Numerics for Brownian dynamics simulations

We hope to draw a connection between the Langevin equation and Brownian dynamic simulation. <mark>These notes closely follow Ref. [27].</mark> We won't delve into any complicated numerical integration scheme; we just want to paint the essential picture. We will start with the Brownian equation of motion

$$\dot{x} = -\zeta^{-1}\left[f(t) + \xi(t)\right], \tag{B.1}$$

where the force $f(t) = -\frac{dU}{dx}$ depends on time and the noise is

$$\langle \xi(t) \rangle = 0 \qquad \langle \xi(t)\xi(t') \rangle = 2\zeta k_B T \delta(t - t'). \tag{B.2}$$

Now, integrating this from t to $t + \delta t$ gives

$$x(t) = x(t + \delta t) - \zeta^{-1} \int_t^{t+\delta t} dt' f(t') + \xi(t'), \tag{B.3}$$

To numerically evaluate this, we need way to handle the delta function in the noise term. We can numerically express this as

$$\delta(t - t') \approx \delta(t, t') = \begin{cases} \frac{1}{\delta t}, & \text{if } t \text{ and } t' \text{ are in the same time step } \delta t \\ 0, & \text{otherwise} \end{cases} \tag{B.4}$$

Thus, upon integration we get

$$x(t) \approx x(t + \delta t) - \zeta^{-1}\delta t \left[f(t) + c(t)\sqrt{\frac{2\zeta k_B T}{\delta t}}\right] \tag{B.5}$$

where $c(t)$ is a random number selected from a distribution with average zero and variance of 1. Typically, we prefer to use a random number is selected randomly from the uniform distribution $r \in [-1/2, 1/2]$ which has a variance of $1/12$. Also, we like to express time in terms of discrete steps. Thus, the position update at some time t_{n+1} is

$$x_{n+1} \approx x_n - \zeta^{-1} \delta t f_n + \sqrt{24 D \delta t} r_n \tag{B.6}$$

where we have used the Einstein relation $D = \frac{k_B T}{\zeta}$. At each time time, f_n is calculated, and r_n is selected. We can quickly see that in the absence of forces, the MSD is

$$\langle x_N^2 \rangle = 24 D \delta t \langle r^2 \rangle N = 2Dt \tag{B.7}$$

after $N = t/\delta t$ steps. In comparison to lattice models where a step can either be $\Delta x \pm l$, a step is randomly selected from a uniform distribution $\Delta x \in [-\sqrt{6 D \delta t}, \sqrt{6 D \delta t}]$ in a Brownian dynamics simulation. Note, that is also common to select a random number from a Gaussian distribution instead of a uniform distribution. In that case, a random step length is selected from a Gaussian distribution with average $\mu = 0$ and variance $\sigma = \sqrt{2 D \delta t}$.

Appendix C

NPC supplement

C.1   Linear solution

The analytical solution for flux can be directly derived in the linear case. For ease of calcula-
tion, we reverse the concentration gradient found in the main text, so that $T(0) = 0$ and $T(L) = T_L$,
allowing us to calculate flux at $x = 0$. The reaction-diffusion equations (3.1, 3.2) at steady state in
the linear limit $N \approx N_t$ are

$$0 = -k_{\text{on}}N_t T + k_{\text{off}}C + D_F \frac{\partial^2 T}{\partial x^2}, \tag{C.1}$$

$$0 = k_{\text{on}}N_t T - k_{\text{off}}C + D_B \frac{\partial^2 C}{\partial x^2}. \tag{C.2}$$

The change of variables $C = C_x + N_t K_A T$ ($K_A = k_{\text{on}}/k_{\text{off}} = 1/K_D$) yields

$$0 = k_{\text{off}}C_x + D_F \frac{\partial^2 T}{\partial x^2} \tag{C.3}$$

$$0 = -k_{\text{off}}C_x + D_B \frac{\partial^2 C_x}{\partial x^2} + N_t K_A D_B \frac{\partial^2 T}{\partial x^2}. \tag{C.4}$$

Substituting $C_x(x) = -\frac{D_F}{k_{\text{off}}}\partial^2 T/\partial x^2$ makes equation (C.4) a fourth-order ODE

$$\lambda^2 \frac{\partial^2 T}{\partial x^2} = \frac{\partial^4 T}{\partial x^4}, \tag{C.5}$$

where $\lambda^2 = k_{\text{off}}(D_F + N_t K_A D_B)/(D_F D_B)$. Solutions to this equation have the form $T(x) = b + mx + fe^{\lambda x} + ge^{-\lambda x}$, where b, m, f and g are constants fixed by four boundary conditions: free
TF concentration is fixed at the edges of the pore, with $T(0) = 0$, $T(L) = T_L$. No flux of bound TF
into or out of the pore occurs, giving $\partial C/\partial x|_{x=0} = 0$, $\partial C/\partial x|_{x=L} = 0$. The constants of integration

are

$$b = -(f + g), \tag{C.6}$$

$$m = \frac{T_L\lambda\left(\zeta - (D_F/k_{\text{off}})\lambda^2\right)\left(e^{L\lambda} + 1\right)}{2\zeta - 2\zeta e^{L\lambda} + L\zeta\lambda - (D_F/k_{\text{off}})L\lambda^3 - (D_F/k_{\text{off}})L\lambda^3 e^{L\lambda} + L\zeta\lambda e^{L\lambda}}, \tag{C.7}$$

$$f = -\frac{\zeta m}{\lambda\left(\zeta - (D_F/k_{\text{off}})\lambda^2\right)\left(e^{L\lambda} + 1\right)}, \tag{C.8}$$

$$g = \frac{\zeta m + f\zeta\lambda - (D_F/k_{\text{off}})f\lambda^3}{\zeta\lambda - (D_F/k_{\text{off}})\lambda^3}. \tag{C.9}$$

where $\zeta = N_t/K_D$. This leads to a concentration profile of bound TFs

$$C(x) = \zeta\left(b + mx + fe^{\lambda x} + ge^{-\lambda x}\right) - (D_F\lambda^2/k_{\text{off}})\left(ge^{-\lambda x} + fe^{\lambda x}\right). \tag{C.10}$$

To determine the selectivity, we calculate the steady-state flux out of the pore $J = -D_F\partial T/\partial x|_{x=0}$,

giving

$$J = -D_F(m + \lambda f - \lambda g) \tag{C.11}$$

$$J = \frac{T_L(D_F^2/k_{\text{off}})\lambda^3\left(e^{L\lambda} + 1\right)}{2\zeta - 2\zeta e^{L\lambda} + L\zeta\lambda - (D_F/k_{\text{off}})L\lambda^3 - (D_F/k_{\text{off}})L\lambda^3 e^{L\lambda} + L\zeta\lambda e^{L\lambda}} \tag{C.12}$$

For a non-binding particle, $C(x) = 0$, $T = T_L x/L$, and

$$J_n = -\frac{D_F T_L}{L}. \tag{C.13}$$

We note that the selectivity J/J_n is then independent of T_L in the linear approximation.

C.2   NPC parameters

We used the length of the pore filled with FGs $L = 100$ nm [105, 142]; $L = 30$ nm gave similar results (data not shown). Total FG Nup concentration was determined from an estimate of the number of TF binding sites (800), and the volume of a cylinder of diameter 60 nm and length, L. The free diffusion coefficient of a TF within the pore was determined from the flux of a non-binding species [94] to be $D_F = 0.012$ μm^2/s. This is a reasonable value, with slower diffusion than that of karyopherins in the nuclear compartment, $D_F = 1$ μm^2/s [143]. The barrier imposed by the FG Nups to a TF and its non-binding counterpart is incorporated into the effective TF concentration

at the edge of the gel. We estimate this barrier ≈ 1.5 $k_B T$ for an NTF2 sized molecule [48]. We estimate the cytoplasmic concentration of NTF2 is 5 μM. Then $T_L = 5 \times e^{-1.5} \mu$M $= 1$ μM. The binding affinity of TFs for FG Nups within the NPC is not well known, and involves a complex interplay between site-specific affinity and change in polymer conformations [113]. Therefore, we consider a range that includes most measurements and estimates of K_D between 10 nM and 10 μM [48, 89, 108, 113, 128, 144].

C.3   Diffusion note

Here, we make the approximation that the diffusion is normal, with $\langle x(t)^2 \rangle \propto t$. In this model, motion is slightly subdiffusive because of the nonlinearity of the equations, and because binding to a random location within a well introduces a fluctuating force. However, in the regimes most relevant to the NPC, where the binding lifetime is short, this effect is minimal.

C.4   Hopping simulation

In our simulation of TF motion with hopping between FG Nups while bound, we represented each FG Nup as an entropic spring (represented by a harmonic potential well). Well positions were randomly chosen from a uniform distribution, with the exception that we always placed one well at the starting position of the TF. The particle (the TF) started the simulation bound to this FG Nup, and remained bound throughout the simulation. While bound to one FG Nup, the TF diffused within the harmonic well representing that FG Nup. We recorded the position and mean-squared displacement of the TF from its starting location, which we then used to determine a bound diffusion coefficient, as described in more detail below. The TF could hop between tethers by changing which well it moved in.

C.4.1   Diffusion in a potential well

The TF moved in the harmonic potential of the FG Nup by Brownian dynamics. TF position updated using a force-dependent diffusive step [145].

$$x(t + \delta t) = x(t) + \frac{F}{\Gamma}\delta t + \delta x, \tag{C.14}$$

where F is the force acting on the particle, Γ is the drag coefficient, δt is the timestep, and δx is a random Brownian step drawn from a Gaussian distribution with variance $\sigma^2 = 2D\delta t$. The drag coefficient of a spherical particle at low Reynolds number is given by Stokes' Law as $\Gamma = 6\pi\eta r$, where η is the fluid's viscosity and r is the sphere's radius. This result can be combined with the Einstein relation $D = k_B T/(6\pi\eta r)$ to give

$$\Gamma = \frac{k_B T}{D}. \tag{C.15}$$

The force $F = -k\Delta x$, where k is the spring constant of the FG Nup and Δx is the displacement of the particle from the Nup attachment point. We model the FG Nup as worm-like-chain at small extension, so that $k = 3k_B T/(2\ell_p L_c)$, where ℓ_p is the tether persistence length and L_c is the contour length. Then

$$x(t + \delta t) = x(t) - \frac{3D\Delta x\delta t}{2\ell_p L_c} + \delta x = x(t) - DK\Delta x\delta t + \delta x, \tag{C.16}$$

where K is the normalized spring constant $K = k/k_B T = 3/(2\ell_p L_c)$.

C.4.2   Hopping probability

We calculated the hopping probability P_{hop} to satisfy the principle of detailed balance. During every iteration of the simulation, we picked an FG Nup at random from a list of the M Nups near enough to have a reasonable probability of hopping. TF hopping to the new FG Nup was attempted with success probability

$$P_{\text{hop}} = r_{\text{hop}}M\delta t e^{-\Delta G/2}. \tag{C.17}$$

Here the base hopping rate r_{hop} is a dimensionless input parameter, and the change in free energy (in units of $k_B T$) between the current Nup and the proposed new Nup is

$$\Delta G = \frac{1}{2} K (x - x_{\text{new}})^2 - \frac{1}{2} K (x - x_{\text{cur}})^2, \tag{C.18}$$

where K is the normalized spring constant, x is the particle's current position, x_{cur} is the anchor location of the Nup to which the particle is currently bound, and x_{new} is the anchor location of the proposed new Nup. Note that when a hop succeeds, the energy landscape changes to that of the new Nup, but the TF's position does not change during the hop. There is no upper bound on P_{hop}, but we adjusted the timestep to ensure that P_{hop} was greater than unity no more than 0.5% of the time that a hop was attempted.

C.4.3   Mean-squared displacement and diffusion coefficient calculation

We ran each simulation for 10^7 time steps with $\delta t = 0.01$ μs, and recorded the particle's position every 100 time steps. We calculated the mean-squared displacement $\langle x^2 \rangle$ (MSD) of the TF and averaged it over 100 runs Figure 4.2A. We then computed

$$\rho_{\text{MSD}}(t) = \langle x^2(t) \rangle \rho(k_{\text{off}}, t) = k_{\text{off}} \langle x^2(t) \rangle e^{-k_{\text{off}} t}, \tag{C.19}$$

as shown in Figure 4.2B, and numerically integrated the distribution in time. We determined the bound diffusion coefficient from the typical MSD-per-binding-event $\overline{\langle x^2 \rangle}$ using

$$D_B = \frac{k_{\text{off}} \overline{\langle x^2 \rangle}}{2}. \tag{C.20}$$

Here, the factor of 1/2 is appropriate because we consider a one-dimensional random walk.

Appendix D

Langevin to Smoluchowski derivation

Here, we present a derivation of the Smoluchowski equation starting from the Langevin equation. The Smoluchowski equation describes the dynamics of the N particle noise ensemble density, $\rho^N(\boldsymbol{r}^N)$ where $\boldsymbol{r}^N = [\boldsymbol{r}_1, \boldsymbol{r}_2, ... \boldsymbol{r}_N]$. The derivation mainly follows Ref. [16]. Our starting place is the Langevin equation

$$\dot{\boldsymbol{r}}_i = \zeta^{-1} \left[-\nabla_i U(\boldsymbol{r}^N) + \boldsymbol{\xi}_i(t) \right], \tag{D.1}$$

where i is the particle label, U is the potential energy from external fields and interactions, and $\boldsymbol{\xi}_i$ is the noise. Assuming the friction is isotropic, homogeneous, and does not mediate hydrodynamic interactions between particles, the noise has the properties *i.e*,

$$\langle \xi_i(t) \rangle = 0 \qquad \langle \xi_i^\alpha(t) \xi_j^\beta(t') \rangle = 2\zeta \delta_{ij} \delta_{\alpha\beta} \delta(t - t'), \tag{D.2}$$

where α, β refer to dimensions and i, j to particle label. First, consider the N particle phase space density $f(\boldsymbol{r}^N, t)$ which describes the probability density of finding particles between $\boldsymbol{r}^N$ and $\boldsymbol{r}^N + \delta r^N$. One may note that, unlike some phase space densities, this does not depend on momentum. This is because we are in the overdamped limit and dropped the inertial term in the Langevin equation. In other words, we are essentially averaging over the momentum degrees of freedom because we assume their dynamics equilibrate on time scales we are not interested in [24].

The probability density is a conserved quantity since the system must always be somewhere in phase space. Therefore, it must obey a continuity equation

$$\frac{df(\boldsymbol{r}^N, t)}{dt} = \frac{\partial f(\boldsymbol{r}^N, t)}{\partial t} + \sum_i \nabla_i \cdot \left[\dot{\boldsymbol{r}}^N f(\boldsymbol{r}^N, t) \right] = 0. \tag{D.3}$$

The equation above in the absence of noise is the Liouville equation [16]. Including noise gives us the Fokker-Planck equation. We will let $\boldsymbol{v}_i = -\nabla_i U(\boldsymbol{r}^N)$, and plug Eqn. D.1 into Eqn. D.3 to get

$$\frac{\partial f(\boldsymbol{r}^N, t)}{\partial t} + \sum_i \boldsymbol{\nabla}_i \cdot \zeta^{-1} \left[f(\boldsymbol{r}^N, t) \left(\boldsymbol{v}_i(\boldsymbol{r}^N) + \boldsymbol{\xi}_i(t) \right) \right] = 0. \tag{D.4}$$

We can separate out the noise term to get

$$\frac{\partial f}{\partial t} = -\mathcal{L}f - \sum_i \boldsymbol{\nabla}_i \cdot \zeta^{-1} \boldsymbol{\xi}_i(t) f, \tag{D.5}$$

where $\mathcal{L} = \sum_i \zeta_i^{-1} \boldsymbol{\nabla}_i \boldsymbol{v}_i$. Integrating with respect to time gives

$$f(t) = e^{-\mathcal{L}t} f(0) - \zeta^{-1} \int_0^t ds\, e^{-\mathcal{L}(t-s)} \sum_i \boldsymbol{\nabla}_i \cdot f(s) \boldsymbol{\xi}_i(s). \tag{D.6}$$

From here, we will plug this back into D.5 and take the noise average $\langle ... \rangle$.

$$\frac{\partial \langle f(t) \rangle}{\partial t} = -L \langle f(0) \rangle + \sum_i \langle \boldsymbol{\xi}_i \rangle_n e^{-\mathcal{L}t} f(0) \tag{D.7}$$

$$- \sum_j \boldsymbol{\nabla}_j \zeta^{-2} \int_0^t ds\, e^{-\mathcal{L}(t-s)} \sum_i \boldsymbol{\nabla}_i \cdot \langle \boldsymbol{\xi}_i(t) f(s) \boldsymbol{\xi}_j(s) \rangle. \tag{D.8}$$

The final step deserves a bit of a explanation. Before we can use the properties of the noise to deal with the integral, we need to think about the $\langle \xi_i(t) \xi_j(s) f(s) \rangle$ term. The term $f(s)$ depends on all of the noise terms at some earlier time, call it $s' < s < t$. The noise terms are all delta-function correlated in time. Thus, there cannot be any correlations between the noise at s and t and phase density at time $f(s)$ because it only depends on noise at earlier times s'. Therefore, $\langle \xi_i(t) \xi_j(s) f(s) \rangle = \langle \xi(t) \xi(s) \rangle \langle f(s) \rangle = \langle \xi(t) \xi(s) \rangle \rho^N(s)$ where $\rho^N(\boldsymbol{r}^N, s) = \langle f(s) \rangle$ is the noise averages phase space probability density. Making this substitution and using properties of the noise we get the Smoluchowski equation,

$$\frac{\partial \rho^{(N)}(\boldsymbol{r}^N, t)}{\partial t} = \sum_i \boldsymbol{\nabla}_i \left[\zeta^{-1} \nabla_i U(\boldsymbol{r}_N) \rho^{(N)}(\boldsymbol{r}^N, t) \right] + \sum_i \boldsymbol{\nabla}_i \cdot D \boldsymbol{\nabla}_i \rho^{(N)}(\boldsymbol{r}^N, t). \tag{D.9}$$

Note that in the absence of fields, we have the diffusion equation. Also, when the potential energy is just from an external field $U(\boldsymbol{r}^N) = \sum_i \phi(r_i)$ we recover the drift-diffusion equation. If more complicated friction tensors are involved, the equation becomes

$$\frac{\partial \rho^{(N)}(\boldsymbol{r}^N, t)}{\partial t} = \boldsymbol{\nabla}_i \left[\zeta ij^{-1} \nabla_j U(\boldsymbol{r}_N) \rho^{(N)}(\boldsymbol{r}^N, t) \right] + \boldsymbol{\nabla}_i \cdot D_{ij} \boldsymbol{\nabla}_j \rho^{(N)}(\boldsymbol{r}^N, t), \tag{D.10}$$

where the sum over indices is implied. I direct the reader to Ref. [24] and references within to obtain this result, but it can be derived from the procedure I just laid out.

Appendix E

Smoluchowski equation to DDFT

This appendix describes how to go from the Smoluchowski equation to a closed form for the one-particle density using dynamic density functional theory. <mark>These steps mainly follow Ref. [24].</mark> The Smoluchowski equation describes the evolution of the N particle density $\rho^{(N)}(\boldsymbol{r}^N, t)$, and it can be derived starting from the Langevin equation (see Appx. D). $\rho^{(N)}(\boldsymbol{r}^N, t)$ describes the probability of finding the particles at $\boldsymbol{r}^N = [\boldsymbol{r}_1, \boldsymbol{r}_2, ... \boldsymbol{r}_N]$ in phase space.

$$\frac{\partial \rho^{(N)}(\boldsymbol{r}^N, t)}{\partial t} = \boldsymbol{\nabla}_i \left[\zeta_{ij}^{-1} \nabla_j U(\boldsymbol{r}_N, t) \rho^{(N)}(\boldsymbol{r}^N, t) \right] + \boldsymbol{\nabla}_i \cdot D_{ij} \boldsymbol{\nabla}_j \rho^{(N)}(\boldsymbol{r}^N, t), \qquad \text{(E.1)}$$

where U is the total potential. In general, this is given by

$$U(\boldsymbol{r}^N, t) = \sum_i^N V_{\text{ext}}(\boldsymbol{r}_i, t) + \frac{1}{2} \sum_{j \neq i}^N \sum_i v_2(\boldsymbol{r}_i, \boldsymbol{r}_j) + \frac{1}{6} \sum_{k \neq j \neq 1} \sum_{j \neq i} \sum_i^N v_3(\boldsymbol{r}_i, \boldsymbol{r}_j, \boldsymbol{r}_k) + ... \qquad \text{(E.2)}$$

where V_{ext} is the potential form external fields and v_n is the n body interaction potential. We are interested in deriving an equation for the one-body density

$$\rho^{(1)}(\boldsymbol{r}) = N \int d\boldsymbol{r}_2 ... \int d\boldsymbol{r}_N \rho^{(N)}(\boldsymbol{r}^N), \qquad \text{(E.3)}$$

where describes the probability of finding a particle at position $\boldsymbol{r}$ irrespective of the other particles' locations. In general, the n particle density—the probability of finding a subset of n particles at position $\boldsymbol{r}^n = [\boldsymbol{r}_1, ... \boldsymbol{r}_n]$—is [50]

$$\rho^{(n)}(\boldsymbol{r}^n) = \frac{N!}{(N-n)!} \int d\boldsymbol{r}_{n+1} \int d\boldsymbol{r}_N \rho^N(\boldsymbol{r}^N, t). \qquad \text{(E.4)}$$

We can integrate the Smoluchowski equation over coordinates $\boldsymbol{r}_2, ...\boldsymbol{r}_N$ to get

$$\frac{\partial \rho^{(1)}(\boldsymbol{r}_1, t)}{\partial t} = \nabla_1 D \nabla_1 \rho^{(1)}(\boldsymbol{r}_1, s) + \zeta^{-1} \nabla_1 \left(\rho^{(1)}(t) \nabla_1 V_{\text{ext}} \right) \tag{E.5}$$

$$+ \nabla_1 D \int d\boldsymbol{r}_2 \rho^{(2)}(\boldsymbol{r}_1, \boldsymbol{r}_2) \nabla_1 v_2(\boldsymbol{r}_1, \boldsymbol{r}_2) \tag{E.6}$$

$$+ \nabla_1 D \int d\boldsymbol{r}_2 \int d\boldsymbol{r}_3 \rho^{(3)}(\boldsymbol{r}_1, \boldsymbol{r}_2, \boldsymbol{r}_3) \nabla_1 v_3(\boldsymbol{r}_1, \boldsymbol{r}_2, \boldsymbol{r}_3) + ... \tag{E.7}$$

This is not a closed equation because the evolution of $\rho^{(1)}$ depends on the higher order densities $\rho^{(2)}, ...\rho^{(n)}$. Evans originally found a way to express the two-body density in terms of the direct correlation function $-k_B T \rho^{(1)}(\boldsymbol{r}_1) \nabla c^{(1)}(\boldsymbol{r}_1) = \int d\boldsymbol{r}_2 \rho^{(2)}(\boldsymbol{r}_1, \boldsymbol{r}_2) \nabla_1 v_2(\boldsymbol{r}_1, \boldsymbol{r}_2)$ for a liquid in equilibrium [137]. This can be generalized for higher order terms [24] to give

$$-k_B T \rho^{(1)}(\boldsymbol{r}_1) \nabla c^{(1)}(\boldsymbol{r}_1) = \sum_n \int r_2 ... \int r_n \rho^{(n)} \nabla_1 v_n(\boldsymbol{r}_n). \tag{E.8}$$

Plugging this into Eqn. E.5 gives a closed form for our equations if direct correlation function $c^{(1)}$ was known—and not dependent on higher order densities. Here is where DDFT comes into play. The direct correlation function in equilibrium can be expressed as a functional derivative of the excess free energy—i.e., free energy contribution from interactions—with respect to the single body free energy [22, 23, 50, 137]

$$c^{(1)}(\boldsymbol{r}) = -\beta \frac{\delta \mathcal{F}^{ex} \left[\rho^{(1)}(\boldsymbol{r}) \right]}{\delta \rho^{(1)}(\boldsymbol{r})}. \tag{E.9}$$

One of the main assumptions is that Eqn. E.8 and Eqn. E.9 are valid for a fluid out of equilibrium [24]. In doing so, we obtain the DDFT equation of motion [22–24, 137]

$$\frac{\partial \rho(\boldsymbol{r}, t)}{\partial t} = \boldsymbol{\nabla} \cdot \left[\zeta^{-1} \rho(\boldsymbol{r}, t) \boldsymbol{\nabla} \frac{\delta \mathcal{F} \left[\rho(\boldsymbol{r}, t) \right]}{\delta \rho(\boldsymbol{r}, t)} \right]. \tag{E.10}$$

where we have dropped the superscript (1) from the one-body density—as is commonly done in the literature. The free energy is separable into contributions from the ideal gas entropy, excess/interactions, and external fields [50]

$$\mathcal{F} = \mathcal{F}^{id} + \mathcal{F}^{ex} + \mathcal{F}^{ext}. \tag{E.11}$$

The challenge of DDFT if the excess free energy is not necessarily a known functional; it typically to be approximated [25]. In summary, the two main approximations of DDFT are: the correlations when the system is out of equilibrium is the same for the equilibrium system at density $\rho(\boldsymbol{r}, t)$ and the functional approximation of the excess free energy. It should also be mentioned that DDFT, although built upon the stochastic Langevin equation, is deterministic [136] because we have taken the noise ensemble average.